Acta Astronautica 240 (2026) 430–447

Contents lists available at ScienceDirect

Acta Astronautica

journal homepage: www.elsevier.com/locate/actaastro

Research paper

Optimal control-based design and feasibility assessment of rendezvous trajectories for 'In-Air Capturing' of a reusable launcher stage

Sunayna Singh [a,*], Marco Sagliano [b,c]

[a] DLR Institute of Space Systems, Robert Hooke Strasse 7, 28359, Bremen, Germany
[b] Department of Industrial Engineering, Via Luciano Montaspro 97, University of Bologna, 47121, Bologna, Italy
[c] Guidance, Navigation and Control Department, Robert Hooke Str. 7, Bremen, Germany

ARTICLE INFO

Keywords:
Optimal control
In-Air Capturing
Reusable launcher technology
Pseudospectral methods
Gain-scheduled LQR

ABSTRACT

'In-Air Capturing' is an innovative mid-air recovery technique where a winged reusable launch vehicle (RLV) is retrieved by a towing aircraft and transported back to the launch site. This approach eliminates landing fuel requirements and increases payload capacity. During 'In-Air Capturing', the RLV must execute a precise rendezvous maneuver and maintain stable formation within a designated, wake-free mating zone behind the aircraft. A tethered capturing device is deployed in advance and awaits connection as the RLV arrives in position. This paper presents a comprehensive trajectory optimisation and control framework for the rendezvous phase, addressing multiple objectives, strict path constraints, capturing device range limits, and external disturbances such as aircraft wake and wind. The trajectory is optimized using Legendre–Gauss–Radau pseudospectral method, with refinement of initial conditions and evaluation of both single- and multiple-capture attempt scenarios. For control, a gain-scheduled Linear Quadratic Regulator (LQR) based on the RLV's energy is developed. To improve robustness, a disturbance observer is integrated into the controller to estimate and correct for wind and wake-induced disturbances during flight. Capture feasibility is assessed through a Monte-Carlo analysis, and the results are used to identify critical boundaries and conditions that determine when re-planning of the guidance trajectory is necessary.

1. Introduction

The 'In-Air Capturing' recovery method was first invented and patented by the German Aerospace Center (DLR) in 2003 [1,2]. In this concept, a winged booster stage is captured mid-air by a towing aircraft (TA), which then returns it to the landing site through a controlled towing operation. The TA effectively acts as an external propulsion system for the reusable launch vehicle (RLV), eliminating the need for onboard descent propellant and thereby reducing overall launch mass. This strategy differs from orbital gliding vehicles, which retain sufficient momentum after separation to perform long-range return maneuvers. Whereas suborbital boosters descend with much less residual energy and cannot return to the launch site on their own without an added propulsion system. For these cases, 'In-Air Capturing' is advantageous, as the TA provides the missing return energy without requiring additional engines or propellant on the booster, making the method theoretically both efficient and cost-effective.

Conventional recovery strategies such as down-range landing (DRL) or return-to-launch site (RTLS) require significant onboard propellant for deceleration and landing maneuvers. Flyback boosters require additional turbofan engines, adding mass and complexity due to the extra propulsion system. Parachute- or parafoil-based mid-air recovery is limited to smaller stages. Other descent concepts such as "dead-leaf", which combine a boostback burn with unpowered glide, have been found to be less performant than flyback approaches [3], but may offer advantages in terms of cost [4]. In the case of 'In-Air Capturing', adding wings and landing gear does increase the structural index (ratio of dry mass to total propellant mass) of the RLV compared to vertical-landing stages. However, the overall inert mass (dry mass plus residual propellants needed for controlled re-entry, landing, or flyback) is still lower because no descent propellant is required. Studies show that 'In-Air Capturing' achieves the lowest inert mass ratio across different propellant choices, with a structural index higher than vertical landing methods but lower than flyback boosters. This means that the added structures are more than balanced by the savings from removing descent propellant, making 'In-Air Capturing' a potentially efficient recovery method. A detailed comparison of various RLV approaches

* Corresponding author.
E-mail addresses: sunayna.singh@dlr.de (S. Singh), marco.sagliano@unibo.it (M. Sagliano).

https://doi.org/10.1016/j.actaastro.2025.12.020
Received 25 August 2025; Received in revised form 13 November 2025; Accepted 8 December 2025
Available online 11 December 2025

based on their performance, size, mass, operational aspects, and complexity is provided in [5], while the cost benefits are evaluated by analysing both recurring and non-recurring expenses using a top-down parametric cost model in [6].

Abbreviations

6DOF Six Degrees of Freedom
ACCD Aerodynamically Controlled Capturing Devices
DLR German Aerospace Center
DRL down-range landing
ELV expendable launch vehicle
FEM finite element method
L/D lift-to-drag
LQR Linear Quadratic Regulator
NLP non-linear programming problem
OCP Optimal Control Problem
RANS Reynolds Averaged Navier–Stokes
RLV reusable launch vehicle
RTLS return-to-launch site
TA towing aircraft
UHMWPE Ultra-High-Molecular-Weight Polyethylene
VisNav Vision-Based Navigation Sensor

List of symbols

C_D Drag coefficient
C_L Lift coefficient
D Aerodynamic drag force in N
J_n Cost function, where the index $n = 1, 2, \dots$
L Aerodynamic lift force in N
R_0 Radius of the Earth in m
S Vehicle reference area in m^2
α Angle of attack in rad
$\boldsymbol{K}_x$ Control gain matrix corresponding to component $x \in \{\mathrm{LQR}, \mathrm{d}\}$ denotes Linear Quadratic Regulator (LQR), or disturbance (d)
$\boldsymbol{\Lambda}$ Costate vector associated with the Hamiltonian
$\dot{x}$ Time derivative of a variable x with respect to time t
γ Flight path angle in rad
$\hat{\mathbf{e}}$ Estimated error or residual
$\hat{\mathbf{x}}$ Estimated state vector
λ Longitude in rad
$\mathbf{A}_d$ Discrete-time state transition matrix representing the linearized system dynamics
$\mathbf{B}_d$ Discrete-time control input matrix defining how control inputs affect the system states
$\mathbf{CovX} \in \{\mathbf{P}, \mathbf{Q}, \mathbf{R}\}$ Generic covariance matrix, where **CovP** denotes the state estimation error covariance, **CovQ** the process noise covariance, and **CovR** the measurement noise covariance
$\mathbf{Q}$ State-weighting matrix in the Linear Quadratic Regulator (LQR) cost function
$\mathbf{R}$ Control-weighting matrix in the Linear Quadratic Regulator (LQR) cost function
$\mathbf{r}_{\mathbf{RLV/TA}}$ Relative position of the RLV in the TA body frame in m
$\mathbf{u}_x$ Component of the control input vector, where $x \in \{\mathrm{ff}, \mathrm{fb}, \mathrm{d}\}$ denotes feed-forward (ff), feed-back (fb), or disturbance (d)
$\mathbf{v}_{\mathbf{RLV/TA}}$ Relative velocity of the RLV in the TA body frame in m/s
$\mathbf{x}$ State vector of RLV in Earth centred frame
$\mathcal{H}$ Hamiltonian function
ω Earth's rotation rate in rad/s
ϕ Latitude in rad
ψ Heading (azimuth) angle in rad
σ Bank angle in rad
g_0 Gravitational acceleration at sea level in m/s^2
m_0 Mass of the RLV in kg
r Radial distance from the center of the Earth in m
v Velocity in m/s
w_n Scalar weight, where the index $n = 1, 2, \dots$

From an environmental perspective, 'In-Air Capturing' also offers advantages compared to propulsive recovery methods. Since no re-entry or landing burns are performed, 'In-Air Capturing' avoids the large amounts of kerosene or methane propellant normally consumed at high altitudes, which are particularly harmful due to black carbon and water vapour emissions in the upper atmosphere [7]. While the TA also consumes fuel, its emissions occur at lower altitudes and are far less damaging than rocket exhaust at stratospheric levels. Studies show that 'In-Air Capturing' increases total exhaust only modestly (about 10%) compared to expendable vehicles, whereas DRL or RTLS can increase exhaust by 27%–40% [8]. Life cycle assessments further confirm that 'In-Air Capturing'-based fleets can achieve lower overall climate impacts than methane-fuelled vertical take-off vertical landing systems, especially when combined with hydrogen propulsion [7].

Fig. 1 illustrates the operational cycle of 'In-Air Capturing'. After stage separation, the winged RLV follows a ballistic descent, then transitions into controlled subsonic glide at 20 km altitude. As it descends further to around 10 km, the TA glides from cruise altitude to initiate a coordinated formation flight. The TA maintains a lead position while the RLV performs a precise rendezvous maneuver (between 8 km and 3 km altitude) to achieve safe proximity behind the aircraft. Meanwhile, a tethered capturing device is deployed from the TA, which trails behind and autonomously docks with the approaching RLV. After docking, the TA throttles up and executes a pull-up maneuver, shifting the combined system from descending flight into a climb prior to reaching 2 km altitude. It then tows the unpowered RLV back to the launch site, where it is released near the airfield to perform an autonomous runway landing. During the tow-back phase, the TA provides the thrust required to overcome the aerodynamic drag of the RLV, while the RLV itself balances its weight through lift generated by its wings. The objective of the tow-back is therefore not to carry the RLV, but simply to provide the range needed to return to the landing site. Close to the runway (distance less than 5 km), the tether between the two vehicles is detached, and the RLV continues to land using its own landing gear.

The current study examines the process from the RLV's rendezvous with the TA up to the moment of capture. Achieving a successful connection between the RLV and the capturing device requires precise coordination among multiple aircraft. The RLV must execute a controlled rendezvous maneuver and position itself directly behind the TA, remaining within the effective range of the capturing mechanism. The range of the capturing device is constrained by both the tether length and the maneuverability of the device itself. Additionally, attempting the capture behind the aircraft exposes the system to strong wake-induced disturbances. Given that the capturing device is much smaller than the other two aircraft, these disturbances can lead to a severe reduction or even a complete loss of control. Hence, the capture must be performed within a carefully planned region that is safe for the operation, referred to as the mating zone in this study.

Additionally, operational safety imposes further constraints on the planned trajectory for the RLV: the RLV's trajectory must maintain a safe separation from the TA to avoid collision hazards and to allow for a feasible abort in case of failure. To improve the chances of a successful capture, multiple capture attempts must be planned; therefore, it is desirable to maximise the time the RLV can remain within the mating zone. Achieving this becomes particularly challenging when the TA and RLV possess different aerodynamic characteristics, leading to mismatches in glide performance, speed envelopes, and maneuverability. To reconcile these competing demands, the rendezvous of the RLV can be formulated as an Optimal Control Problem (OCP), in which the trajectory is optimized to balance safety constraints, maximise capture opportunities, and compensate for aerodynamic disparities between the vehicles.

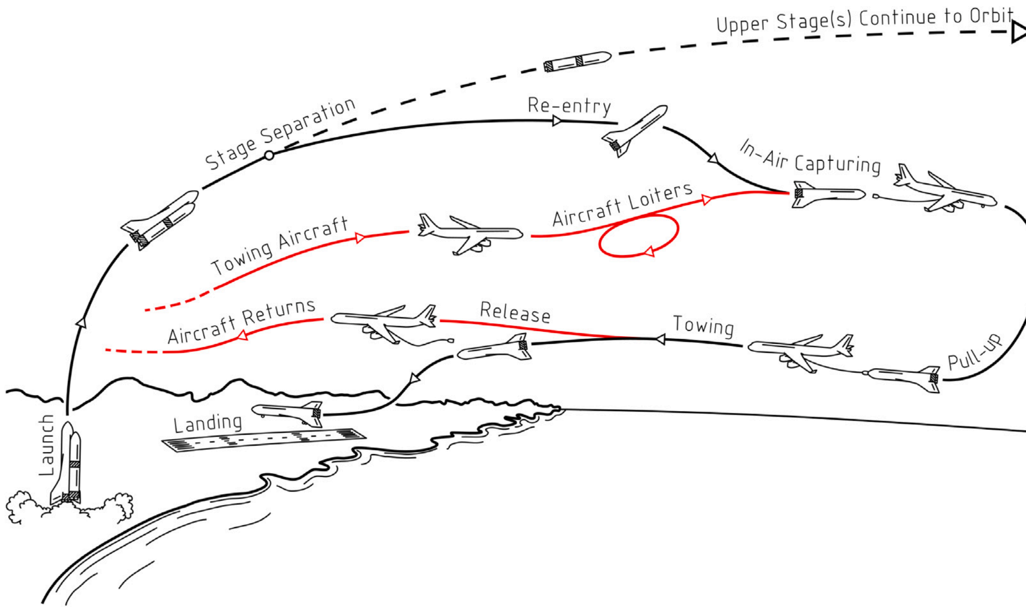

Fig. 1. Schematic of the complete 'In-Air Capturing' mission cycle.

Due to the unique nature of 'In-Air Capturing', no existing literature fully addresses the combined challenges of mid-air recovery involving an unpowered, gliding stage. While aerial refuelling provides a loose analogy in terms of mid-air rendezvous, the underlying dynamics and control requirements differ substantially. 'In-Air Capturing' involves docking an unpowered RLV with limited maneuverability during a low energy glide, requiring precise temporal and spatial coordination in the mating zone behind the gliding aircraft. This places stringent demands on both the guidance system and the control authority of the RLV. Hence, this paper aims to realistically formulate the rendezvous trajectory of the RLV, and optimize it using established advanced optimisation techniques based on pseudospectral methods. The initial states at the start of the maneuver are included as decision variables, allowing the optimisation to adjust both the trajectory and its starting conditions.

The framework further evaluates and optimizes trajectory scenarios involving both single and multiple capture attempts. To demonstrate feasibility under realistic operating conditions, the optimized trajectory is used as a reference for the guidance system and embedded within a closed-loop control framework. A gain-scheduled Linear Quadratic Regulator (LQR) [9–12], based on the RLV's energy state, is employed for trajectory tracking across the wide flight envelope. To enhance robustness against environmental disturbances, a disturbance observer is integrated into the feedback loop. The system is tested under modelled disturbances and uncertainties, and the resulting performance is evaluated to determine the robustness of the approach and to identify critical boundaries for guidance re-planning. This integrated optimisation, guidance, control and validation framework represents a novel step toward making 'In-Air Capturing' a viable and implementable recovery strategy for future reusable launch vehicles.

This paper is organised as follows. Chapter 2 introduces the full-scale vehicles involved in 'In-Air Capturing' and the associated key properties such as aerodynamics. It also defines essential mission concepts, including formation flight requirements and the mating zone, to provide a clear understanding of the problem. Here the overall capture approach is also explained. Chapter 3 addresses the optimisation problem, presenting the RLV equations of motion and the formulation of the OCP, followed by a discussion of the optimisation results. Chapter 4 presents the integrated guidance and control system in closed loop. The optimized trajectory serves as the guidance reference, while a closed-loop control architecture is introduced to counteract uncertainties and disturbances. The chapter analyses closed-loop performance and continues with a Monte Carlo study to assess robustness under non-ideal conditions and to establish operational boundaries. Finally, Chapter 5 concludes the study with some remarks and insight about the work performed. A brief outlook on future developments is also presented here.

2. In-Air Capturing system

In a standard full-scale 'In-Air Capturing' case study, three vehicles are involved: the launcher stage to be recovered, the aircraft for towing operations, and an autonomous capturing device that connects the two vehicles. The vehicles considered in this study — previously selected in [13,14] — are briefly described in Section 2.1. The RLV rendezvous trajectory has two main objectives: first, to enter formation flight with the TA and second, to reach and maintain its position in the mating zone, maximising time within the device's operational reach for docking operation. While formation flight has been studied previously [14–16], existing work is preliminary and requires refinement to make its realisation potentially viable. Section 2.2 discusses its limitations and defines new criteria. The mating zone is then introduced in detail, outlining its purpose, constraints, and key factors influencing its role in the final capture phase. In Section 2.3, the capture mission design is explained, defining the distinct roles of the RLV and the capturing device during the maneuver.

2.1. Full-scale test cases

During 'In-Air Capturing', the characteristics of the RLV mainly drive the requirements for the TA and the capturing device. For this research, the RLV is chosen to be the first stage of a 3 stage-to-orbit launch vehicle concept. The returning winged stage, designated RLVC4-IIIB, features a unique swept-wing configuration as explained in [17]. During hypersonic re-entry, the spacecraft's outer wings are folded to prevent shock-shock interactions. Once the vehicle decelerates to subsonic speeds, the outer wings are deployed, as illustrated in Fig. 2. The larger wings enable a higher maximum trimmed lift-to-drag (L/D) ratio of up to 6 in the subsonic regime (as shown in Fig. 3), making this configuration suitable for 'In-Air Capturing' [14]. The control is performed using flaps on the wings that can be deflected

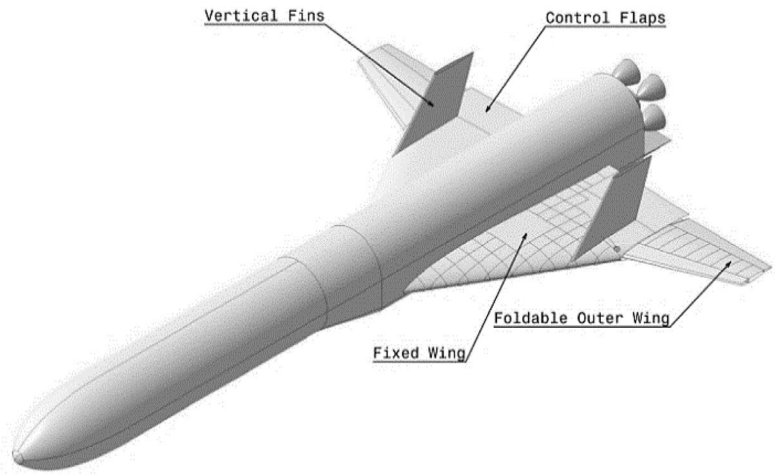

Fig. 2. Reusable launch vehicle — RLVC4-IIIB — with deployed outer wings for higher subsonic aerodynamic performance [13].

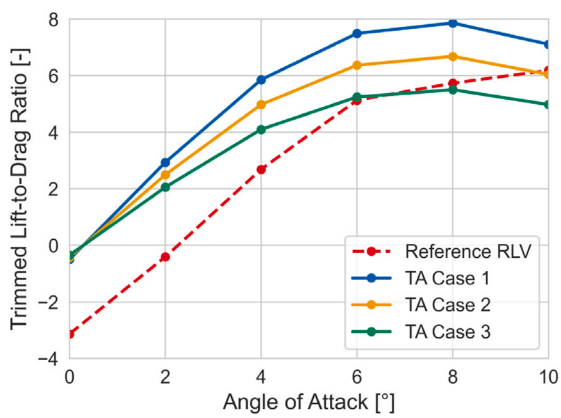

Fig. 3. Aerodynamic performance of RLV (with deployed outer wings) and different TA configurations (with added drag) as a function of angle of attack.

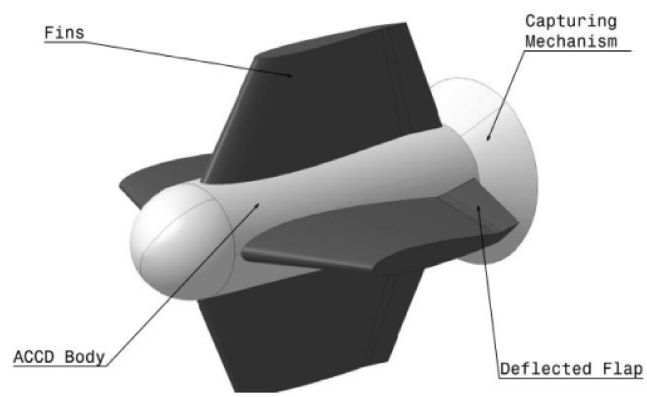

Fig. 4. Aerodynamically Controlled Capturing Device (ACCD) [13].

±20°. Although the original RLV was designed for recovery with 'In-Air Capturing', it was not specifically optimized for it. Design targets include a landing speed of ≤105 m/s and a landing-gear box placement that allows ≈12° angle of attack during landing. The dry mass is approximately 70 tons, with about 10 tons of residuals and reserves included as margin. A detailed mass distribution, ascent trajectory of the complete launch vehicle, and performance comparison to European expendable launch vehicle (ELV)s are provided in [17]. During descent, the RLV is expected to weigh approximately 80 tons. The dispersion in descent trajectories until the beginning of the rendezvous and mission profile have been studied in [16]. Through the current study, the goal is to also identify and characterise limitations and requirements of the RLV to guide subsequent design iterations and improve its suitability for 'In-Air Capturing'.

For capturing the large rocket stage, a suitably sized TA is essential. The retired jetliner Airbus A340-600 [18] has been chosen due to its substantial loading capacity and thrust. Equipped with four Rolls-Royce Trent 556 engines and an advanced flight control system, the A340-600 meets the specifications for 'In-Air Capturing' of RLVC4-IIIB. To achieve prolonged formation with the RLV, the aerodynamic performance between the two vehicles must be comparable. However, typical long-range commercial aircraft tend to have a lift-to-drag (L/D) ratio of up to 20. This performance gap is reduced by deploying drag generating surfaces like spoilers and landing gear. A detailed study for the selection of the most suited TA configuration can be found in [14]. The selected configuration (see TA Case 1 in Fig. 3) has a maximum L/D ratio of 8 and weighs approximately 280 tons. In TA Case 1, drag is increased by extending the nose and main landing gear and deflecting the spoilers to −20° (maximum possible deflection −30°)

It can be observed from Fig. 3 that the aerodynamic performance of the previously selected TA configuration (TA Case 1) differs significantly from that of the reference RLV [19]. As a result, maintaining prolonged formation flight to enable multiple capture attempts becomes challenging [14,15]. To better assess the feasibility of the concept and investigate more favourable conditions, two additional configurations with aerodynamic characteristics more closely aligned to the reference RLV are included in this study. In TA Case 2, the base drag is increased by 17.7% across all angles of attack, while in TA Case 3, it is increased by 35%. Although TA Case 3 provides the closest match to the reference RLV's performance, TA Case 2 is considered more achievable, while still being challenging and conservative (as further explained in Section 4). These cases are included to explore the concept's limits and help define the operational boundaries.

Lastly, Fig. 4 illustrates the configuration of the chosen capturing device for 'In-Air Capturing', referred to as the Aerodynamically Controlled Capturing Devices (ACCD). It measures 2 m in length with a cross-sectional diameter of 1.5 m, including the fins. Equipped with four flaps capable of deflecting up to a maximum of ±15°, it provides 6DOF agility and control. Pitch commands use symmetric deflection of the horizontal flaps, yaw uses the vertical pair, and roll is generated by coordinated deflection of all four flaps; asymmetric combinations allow simultaneous motion in all three axes via superposition. A winch on the TA adjusts tether length — typically 150–300 m in this study.

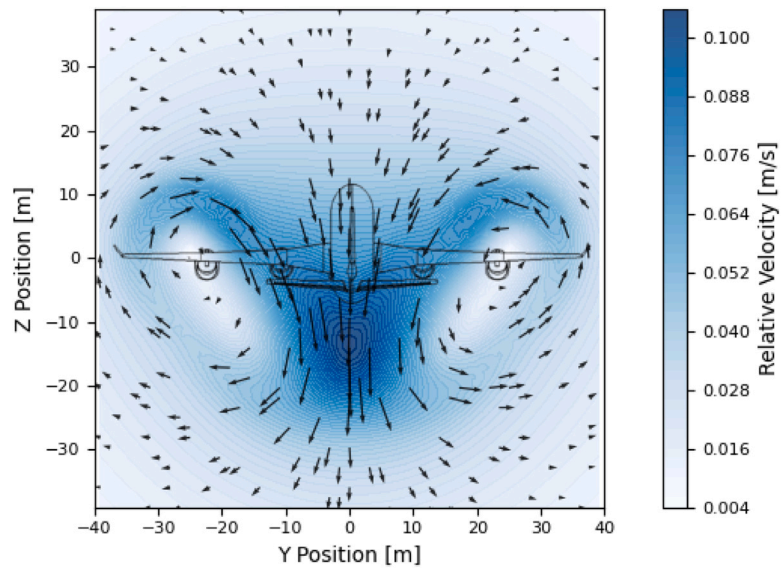

Fig. 5. Wake velocity contours 250 m behind the aircraft [23].

The reference full-scale ACCD weighs ≈ 165 kg. Its nose is tethered to the TA, and an aft-mounted capturing mechanism locks onto a boom on the RLV to form a secure connection. The capturing mechanism at the aft end also functions as a drogue/drag cone, stabilizing the device and helping keep the tether under positive tension to minimize slack during approach. A detailed overview of the capture system, including the aerodynamic performance, modelling of the tether and electro-mechanical design of ACCD can be found in [13,20,21] respectively. The capturing system design accounts for interaction forces and towing loads, as well as mass and power requirements during 'In-Air Capturing' [22].

2.2. Formation flight and mating zone

The 'In-Air Capturing' maneuver begins when the RLV is assumed to be sufficiently close to the TA, with an initial relative distance of approximately 1.5 km. To initiate the capture sequence, the TA descends from its cruise altitude and transitions into a coordinated gliding formation with the RLV. During this phase, the TA maintains a lead position, while the RLV executes a rendezvous maneuver to align its trajectory with the aircraft's flight path, ensuring proper coordination and maintaining a safe separation. This stage, referred to as formation flight, provides the operational window during which the final approach towards the TA and capture attempt is performed.

In previous studies, preliminary formation flight criteria was defined for 'In-Air Capturing' as presented in [14]. Simulations were performed using a 3DOF model with active control systems implemented for both the RLV and the TA. In these simulations, the RLV followed a gliding trajectory with a maximum descent flight path angle of −8°, while the aircraft attempted to match its speed and altitude. The results showed that the formation flight requirements could be maintained for a limited duration — approximately 70 s — due to aerodynamic performance differences between the vehicles [14]. While this window may be sufficient for a successful capture, the study was likely overly optimistic and preliminary. Several critical factors — such as disturbances due to aircraft wake, the maneuverability range of ACCD, and limitations in the range of the relative navigation system — were not considered, thereby reducing the reliability and applicability of the initial criteria. This motivates the need for a more comprehensive formulation of the problem and refined flight strategies.

Additional studies on 'In-Air Capturing' have provided valuable insights into other subsystems that may influence the formation flight criteria:

1. *Aircraft Wake:* A CFD study on the aircraft's wake behaviour [13,19] indicates that significant disturbances can extend up to 350 m from the aircraft's nose. Fig. 5 illustrates the wake's lateral and vertical velocity disturbances at 250 m behind the TA, assuming a 10° angle of attack at 6000 m altitude. Since the capture is expected to occur behind the TA, both the RLV and ACCD are likely to be influenced by these wake effects. Prior studies show that the RLV experiences transient angle-of-attack disturbances but stabilizes quickly [14], whereas the smaller ACCD loses control entirely when exposed [24]. Therefore, to ensure a successful capture, it is critical to attempt the mating or docking maneuver outside the most turbulent regions of the wake.
2. *Maneuverability of ACCD:* The ACCD is connected to the TA by a 250 m Ultra-High-Molecular-Weight Polyethylene (UHMWPE) tether, which stabilizes roughly 50 m below the aircraft and defines the basic capture range. Its maneuverability, assessed through aerodynamic modelling and steady-state tow analysis [20,21], allows displacements of up to about 200 m vertically and laterally at maximum deflection of ±15°. However, not all of these positions behind the TA are practically accessible: some region is strongly affected by the aircraft wake, while the tether attachment near the central landing gear leads to interference of the tether with the airframe at certain angles. To illustrate this, Fig. 6 highlights feasible positions of the ACCD in green and inaccessible ones in red, thereby indicating the limits of the actual docking envelope. In full-scale operation, a winch system can adjust the nominal 250 m tether length between 150 and 300 m, offering additional flexibility during the capture phase.
3. *Close-Range Navigation:* A key aspect of 'In-Air Capturing' is the ACCD's autonomous navigation for docking with the launcher. This requires close-range sensors with at least 35 cm positional and 1° orientational accuracy. A Vision-Based Navigation Sensor (VisNav) is employed to measure relative states between the ACCD and RLV, with GPS/INS/VisNav data fused for accuracy and robustness [25]. However, the VisNav system requires line-of-sight and has an effective range of approximately 200 m, further constraining the RLV's path during final approach.

Accordingly, the formation flight relative distance criterion — previously defined relative to the TA — is updated. The lower bound is set by the minimum tether length (150 m) and the upper bound by the VisNav range (200 m relative to the ACCD). The relative-velocity

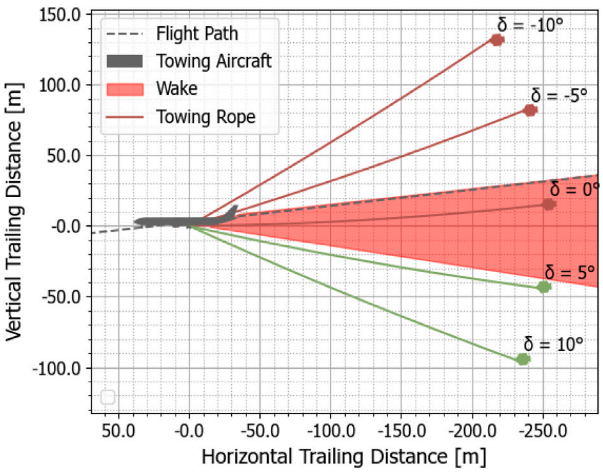

Fig. 6. Maneuverability margin of ACCD at different flap deflections (δ) generated using static force balance [21].

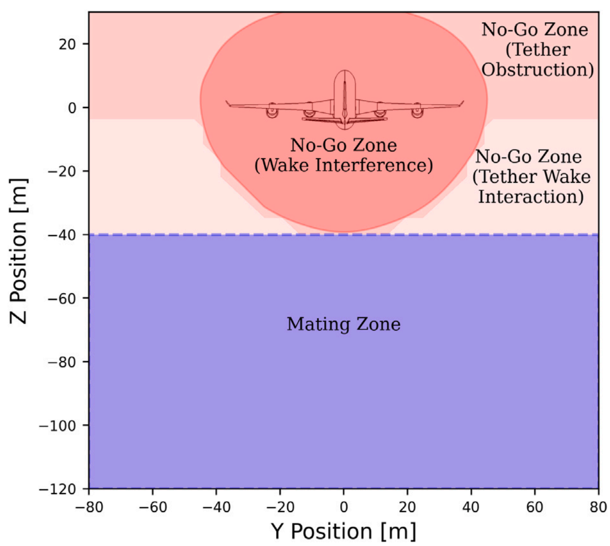

Fig. 7. Mating zone for the docking maneuver between ACCD and RLV relative to TA.

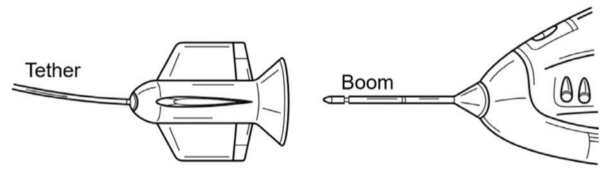

Fig. 8. Schematic of the ACCD and the RLV during capture phase.

constraint is now defined with respect to the ACCD, which can tolerate docking speeds up to 5 m/s [21]. This constraint applies mainly at the time of capture and can be partially corrected by the ACCD itself. Minimising relative velocity with respect to the TA remains important for prolonged formation, but the achievable minimum depends on the TA's aerodynamic configuration (Fig. 3) and should not be treated as a strict constraint. Finally, towards the end of formation flight, the RLV must enter the designated mating zone, where docking is initiated.

The mating zone refers to a designated region behind the TA that is considered the most suitable location for docking. Within this zone, the ACCD positions itself and awaits the arrival of the RLV before initiating the final docking procedure. The boundaries of this zone are determined by three primary factors: the length of the tether, the effect of TA wake, and the maneuverability range of the ACCD. Based on these considerations, a suitable mating zone can be defined. Fig. 7 illustrates the projected No-Go regions along with the designated mating zone nominally located 250 m behind the TA centre of gravity. In the No-Go zones, docking is infeasible due to strong wake turbulence or tether obstruction by the TA body, which limits the ACCD's vertical and lateral maneuverability. The mating zone is positioned to avoid these constraints and provides favourable conditions for docking. This zone spans from 40 m to 120 m below the TA and extends 80 m laterally on each side. For simplicity, it is assumed to have a rectangular shape.

2.3. Capture phase

While the RLV begins formation flight and attempts to arrive at the mating zone, the ACCD positions itself at the projected arrival point of the RLV in the mating zone. It continuously adjusts its orientation and position while handling disturbances from wind and other environmental factors. The goal is to minimize the movement of the capturing device to avoid causing tether vibrations. Through relative navigation and communication between the ACCD and RLV, a coordinated capture can be achieved.

The goal is for the RLV's boom to lock into the ACCD's docking cone (see Fig. 8). A final positional accuracy of 35 cm — slightly smaller than the cone opening — is set for docking [25]. By waiting at the projected arrival point, the ACCD can make its first capture attempt as soon as the RLV enters the mating zone. Prior studies that account for tether vibrations and their damping indicate the ACCD can translate up to 15 m in both the Y and Z directions within 15 s [24]. Therefore, if the RLV remains in the mating zone for more than 15 s, a second capture attempt could be feasible. Adding rope-length flexibility via a winch further increases the chances of making that second attempt.

Capture requires coordination between both vehicles. Given the RLV's limited maneuverability, mission design prioritises arrival and station-keeping in the mating zone. The ACCD takes the more active role during capture, correcting residual errors in relative position and velocity to minimize interaction forces. Accordingly, this study focuses on RLV-side requirements: (i) optimising the approach and station-keeping trajectory to maximize dwell time in the mating zone, and (ii) controlling the RLV to track this trajectory robustly despite disturbances and uncertainties. As a first design iteration, the results establish performance targets, margins, and constraints for subsequent RLV iterations. Future work will cover guidance and control of the capturing device and integrated capture simulations with the navigation module to assess overall feasibility.

3. Trajectory optimisation

This section addresses the optimisation problem itself. In this study, pseudospectral methods are chosen to solve the optimisation problem, given their well-established prominence in addressing complex OCPs. They provide fast and accurate solutions, making them particularly valuable for generating guidance trajectories and enabling path replanning in reusable launch vehicle applications [26–30]. The optimisation is carried out with an hp-adaptive Legendre–Gauss–Radau pseudospectral method [26,27], implemented in a MATLAB-based framework [31]. This method transcribes the continuous-time OCP into a sparse nonlinear programming problem (NLP), which is then solved with advanced solvers such as IPOPT or SNOPT. The Legendre–Gauss–Radau scheme was selected for its favourable handling of boundary conditions and robust convergence properties [32], making it particularly well suited to the demands of the present application.

Hence, the OCP for the RLV rendezvous trajectory is formulated based on the revised formation flight criteria and mating zone requirements, in a manner compatible with pseudospectral method used in the study. The TA trajectory is assumed fixed throughout the optimisation. Although it differs across the TA configurations shown in Fig. 3, it remains constant within each case, and the RLV trajectory is optimized taking the relative TA trajectory into consideration. Section 3.1 introduces the governing equations of motion, Section 3.2 specifies the objectives and path constraints, and Section 3.3 presents the optimized RLV trajectories for each TA configuration.

3.1. RLV equations of motion

For optimisation of the RLV trajectory, the standard point-mass dynamics of the unpowered vehicle over a spherical rotating Earth are described by the following equations of motion [33], assuming no wind and no mass variation.

$$\dot{r} = v \cdot \sin(\gamma) \tag{1}$$

$$\dot{\phi} = \frac{v \cdot \cos(\gamma) \cdot \cos(\psi)}{r} \tag{2}$$

$$\dot{\lambda} = \frac{v \cdot \cos(\gamma) \cdot \sin(\psi)}{r \cdot \cos(\phi)} \tag{3}$$

$$\dot{v} = -\frac{D}{m} - \frac{\mu}{r^2} \cdot \sin(\gamma) + \omega^2 \cdot r \cdot \cos(\phi) \cdot (\sin(\gamma) \cdot \cos(\phi) - \cos(\gamma) \cdot \cos(\psi) \cdot \sin(\phi)) \tag{4}$$

$$\dot{\gamma} = \frac{L \cdot \cos(\sigma)}{m \cdot v} + \frac{v}{r} \cdot \cos(\gamma) - \frac{\mu}{v \cdot r^2} \cdot \cos(\gamma) + 2 \cdot \omega \cdot \sin(\psi) \cdot \cos(\phi) + \frac{\omega^2 \cdot r}{v} \cdot \cos(\phi) \cdot (\cos(\gamma) \cdot \cos(\phi) + \sin(\gamma) \cdot \cos(\psi) \cdot \sin(\phi)) \tag{5}$$

$$\dot{\psi} = \frac{L \cdot \sin(\sigma)}{m \cdot v \cdot \cos(\gamma)} - \frac{v}{r} \cdot \cos(\gamma) \cdot \sin(\psi) \cdot \tan(\phi) + 2 \cdot \omega \cdot (\tan(\gamma) \cdot \cos(\psi) \cdot \cos(\phi) - \sin(\phi)) + \frac{\omega^2 \cdot r}{v \cdot \cos(\gamma)} \cdot \sin(\psi) \cdot \sin(\phi) \cdot \cos(\phi) \tag{6}$$

Here, r is the radial distance from the centre of the Earth to the vehicle, λ and ϕ denote the longitude and latitude, respectively, v is the Earth-centred velocity, γ is the flight path angle, and ψ is the heading angle of the relative velocity vector, measured clockwise from geographic north. The terms D and L represent the aerodynamic drag and lift forces, respectively and are defined as:

$$L = \frac{1}{2} \rho v^2 S C_L \tag{7}$$

$$D = \frac{1}{2} \rho v^2 S C_D \tag{8}$$

Here, C_L and C_D represent lift and drag coefficients respectively, which are functions of the angle of attack and Mach number. Also, ρ represents atmospheric density and S is the reference area of the RLV.

To enhance numerical stability during the optimisation process, all variables in these equations are expressed in a non-dimensional form. All lengths are scaled by the Earth's radius, $R_0 = 6378.137$ km. Time is scaled by $\sqrt{R_0/g_0}$, where $g_0 = 9.80665$ m/s^2 is the gravitational acceleration at the Earth's surface. Consequently, linear velocity is scaled by $\sqrt{g_0 R_0}$, and the Earth's rotation rate ω is non-dimensionalized by $\sqrt{g_0/R_0}$. Therefore, the gravitational acceleration constant g becomes equal to one in the scaled equations. Furthermore, all mass-related terms are scaled by the nominal reference vehicle mass, $m_0 = 79182.58$ kg. It should be noted that the non-dimensionalisation is applied solely for the numerical simulations; the equations and data presented in the following sections correspond to the full-scale system.

The rate of change of angle of attack ($\dot{\alpha}$) and bank angle ($\dot{\sigma}$) are selected as the control variables, denoted by U_α and U_σ, respectively. This modelling choice promotes smoother and more physically realistic trajectories, avoiding abrupt changes in angle of attack (α) and bank angle (σ).

$$\dot{\alpha} = U_\alpha, \quad \dot{\sigma} = U_\sigma \tag{9}$$

This structure improves numerical stability and convergence in direct methods based on pseudospectral collocation, facilitates the inclusion of actuator rate constraints as path constraints, and simplifies the analysis of the Hamiltonian, which is useful for verifying optimality conditions (discussed later in Section 3.3) [34].

Thus, the state vector becomes:

$$\mathbf{x} = [r,\ \phi,\ \lambda,\ v,\ \gamma,\ \psi,\ \alpha,\ \sigma]^T \tag{10}$$

and the control vector becomes:

$$\mathbf{u} = [\dot{\alpha},\ \dot{\sigma}] \tag{11}$$

Table 1
Weights for objective function.

w_1	w_2	w_3	w_4	w_5	w_6	w_7
5	10^{-3}	10	10	100	10^{-7}	10^{-8}

3.2. Optimal control problem

To formulate the cost function for the OCP that would be used for optimisation, the following requirements based on the new criteria for formation flight must be taken into account:

1. During formation, the RLV must approach the TA from behind and starting at a higher altitude.
2. Formation flight must occur within an altitude range of 3000 m to 8000 m.
3. The formation phase begins when the relative distance between the RLV and TA is 450 m.
4. By the end of the formation flight, the RLV should reach a designated mating zone at a relative distance of 250 m from the TA.
5. The relative velocity of the RLV with respect to the TA must be minimized to enable the RLV to remain within the mating zone for an extended duration.
6. Control surfaces must remain unsaturated throughout the formation flight phase.

Cost function

While Requirements 1 and 2 can be satisfied by imposing bounds on the initial and final states of the RLV (as discussed in Section 3.3), a cost function must be introduced to address the remaining requirements and formulate the OCP. The cost function can be divided into three main components such that:

$$J = J_1 + J_2 + J_3 \tag{12}$$

These can be summarized as follows:

- J_1: Minimize overall error in relative state and relative velocity

$$J_1 = \int_{t_0}^{t_f} \left[w_1 \cdot \left\| \mathbf{r}_{\mathrm{RLV/TA}}(t) \right\|^2 + w_2 \cdot \left\| \mathbf{v}_{\mathrm{RLV/TA}}(t) \right\|^2 \right] dt \tag{13}$$

where $\mathbf{r}_{\mathrm{RLV/TA}}(t)$ and $\mathbf{v}_{\mathrm{RLV/TA}}(t)$ are the relative position and relative velocity of RLV in the TA body frame at a given time (t). w_1 and w_2 are weights given in Table 1. Maintaining a close match in these two parameters is essential for achieving formation flight; therefore, medium weights are assigned to this cost function. As noted in Section 2.2, aligning the velocities is advantageous for sustaining long-duration formation flight, but it is not critical since the capturing device can partially compensate for any mismatch. Hence, it is assigned smaller weights compared to the relative position. This cost function addresses criteria 3, 4 and 5 in the new formation flight requirements.

- J_2: Hit the target mating zone conditions
  The mating zone is primarily characterised as a rectangular region located behind the aircraft, bounded in both the relative lateral and relative vertical directions as shown in Fig. 7. Here, the cost function is modelled using a tanh-based soft penalty formulation [35], which increases the cost when the RLV deviates from the boundaries of the mating zone and returns zero when the RLV remains within the zone. A soft penalty is introduced primarily because pseudospectral methods require smooth, differentiable dynamics; discrete or non-differentiable constraints tend to degrade convergence.

$$J_2 = \int_{t_0}^{t_f} \left[w_3 \cdot \zeta(x(t), l_x, u_x) + w_4 \cdot \zeta(y(t), l_y, u_y) + w_5 \cdot \zeta(z(t), l_z, u_z) \right] dt \tag{14}$$

  where x, y, and z represent the relative position components of the RLV in the TA body-fixed frame, and l_i, u_i denote the lower and upper bounds for each direction ($i \in \{x, y, z\}$). w_4, w_5 and w_6 are weights given in Table 1. This cost function is assigned the highest weights, as the RLV's successful arrival in the mating zone is critical for capture. The cost function effectively enforces requirement 5 of formation flight.
  The soft penalty function (ζ) is defined as:

$$\zeta(s(t), l, u) = \alpha \cdot \tanh^2\left(\beta(l - s(t))\right) + \alpha \cdot \tanh^2\left(\beta(s(t) - u)\right), \tag{15}$$

  where s is the current value of the state component (e.g., x, y, or z), and α, β are positive constants that control the weight and sharpness of the penalty.
- J_3: Smoothness penalty on control variables

$$J_3 = \int_{t_0}^{t_f} \left(w_6 \cdot U_\alpha^2 + w_7 \cdot U_\sigma^2 \right) dt \tag{16}$$

  This term applied to the control variables (see Eq. (9)), to encourage gradual variations over time. w_6 and w_7 are weights given in Table 1. The weights in this cost function are chosen small enough to guarantee smoothness of controls, while not impacting the solution significantly. This helps meet requirement 6 of the formation flight.

Constraints

Since the objective function minimizes the relative position of the RLV, an additional path constraint is required to ensure that the minimum allowable distance is not violated. Specifically, this constraint enforces that the relative distance between the RLV and the TA remains greater than or equal to the minimum separation defined by the boundaries of the mating zone (as specified in requirement 4). The upper bound corresponds to the initial maximum relative distance at the start of the rendezvous maneuver.

$$250 \leq \mathbf{r}_{\mathrm{RLV/TA}}(t) \leq 1500, \quad \forall t \in [t_0, t_f] \tag{17}$$

3.3. Numerical simulations

With the objective of achieving formation flight and maximising time spent within the mating zone, the RLV rendezvous trajectory is optimized for three TA configurations (Fig. 3). TA Case 1 exhibits the largest deviation from the RLV, TA Case 2 is moderately similar, and TA Case 3 closely matches the RLV at certain angles of attack. Since 'In-Air Capturing' is very sensitive to aerodynamic similarity between the RLV and TA [14], these cases enable the evaluation of both single- and multiple-attempt rendezvous strategies. The TA reference trajectories for each case are generated using the dynamic model presented in [14]. All TA configurations start from the same initial position but descend along different fixed flight path angles based on the aerodynamic performance. The initial conditions for the TA are summarized in Table 2.

Table 2
Trajectory optimization — TA initial state and bounds for the RLV initial state.

State variable [Unit]	TA initial	RLV initial state bounds	
		Lower	Upper
Altitude [m]	8163.95	8213.95	9163.95
Longitude [°]	−46.1076	−46.1026	−46.0976
Latitude [°]	4.9794	4.9794	4.9794
Velocity [m/s]	213.90	183.90	233.90
Flight path angle [°]	−5.5/−7/−8.5	−12	−6
Heading angle [°]	90	90	90
Angle of attack [°]	8	6	12
Bank angle [°]	0	90	90

Table 3
Trajectory optimisation — Final state bounds for the RLV state.

State variable [Unit]	RLV Final State Bounds	
	Lower	Upper
Altitude [m]	1500	5000
Longitude [°]	−90	90
Latitude [°]	−90	90
Velocity [m/s]	100	200
Flight path angle [°]	−14	−4
Heading angle [°]	0	180
Angle of attack [°]	0	12
Bank angle [°]	−30	30

The OCP is formulated as a single-phase problem, with the RLV assumed to be relatively close to the TA at the start of the simulation. Since principal components of the problem depend on the RLV's position and velocity relative to the TA, the initial conditions for the RLV are defined based on the TA's state. Table 2 summarizes the bounds of the RLV's initial state (relative distance less than 1500 m). Allowing a range of initial conditions enables the optimisation to determine the most favourable starting point for the rendezvous. Since the RLV exhibits poorer aerodynamic performance than the TA in all cases, it is expected to descend with a steeper flight path angle. Therefore, a higher initial altitude margin relative to the TA is selected for the RLV trajectory optimisation. Likewise, the FPA margin is set lower than that of the best-performing TA case. The longitude margin is chosen to ensure that the RLV always approaches the TA from behind, while the latitude margin is fixed to a single value under the simplifying assumption that both trajectories follow an eastward path with a constant azimuth of 90° measured from the North.

The final state of the RLV is defined with relatively loose bounds, independently of the TA state, as summarized in Table 3. The total simulation time is fixed at 250 s to match the final time of the reference TA trajectory. The control rates — the rate of change of angle of attack and bank angle — are bounded between ±5°/s. The TA reference trajectory is provided as a guess for each case. With this setup, the optimisation results for the RLV rendezvous trajectory are presented as follows.

Case 1

Fig. 9 shows the rendezvous of the RLV with TA Case 1. The altitude–velocity profile (top figure) indicates only a small overlap between the RLV and TA trajectories, likely due to the significant difference in aerodynamic performance (see Fig. 3). A closer look at the relative position and velocity of the RLV with respect to the TA, shown in Fig. 9, indicates that formation flight — highlighted by the green shaded region — is maintained for only 70 s. This phase begins at a relative distance of 450 m and continues until the RLV reaches the minimum allowable separation of 250 m. At this point, the RLV is expected to hold its position within the designated mating zone behind the TA, as described in Section 2.2.

Fig. 10 shows the relative X, Y, and Z positions of the RLV with respect to the TA during the rendezvous. The bounds of the mating zone are indicated by red dashed lines in the lateral (Y) and vertical

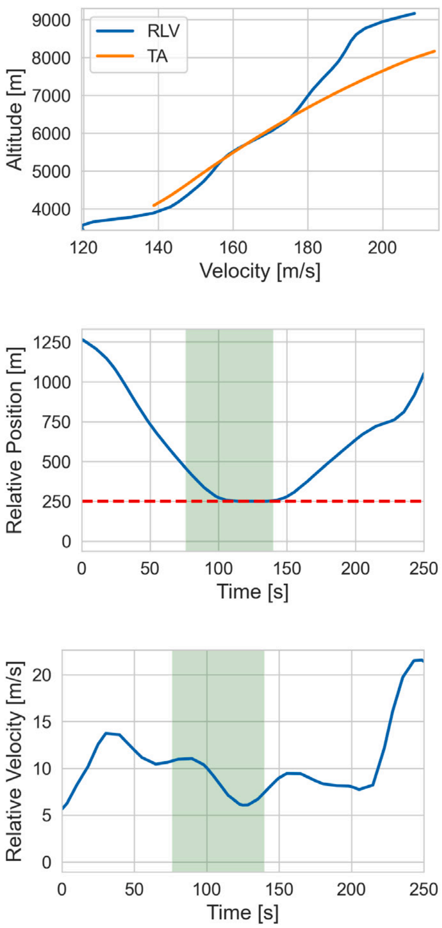

Fig. 9. Rendezvous trajectory simulation of the RLV with TA Case 1.

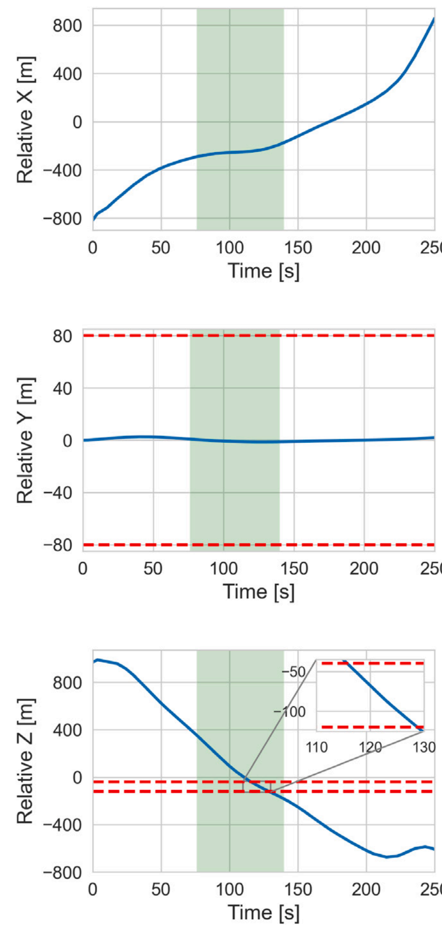

Fig. 10. Position of RLV relative to TA Case 1 with mating zone (red-dash). (For interpretation of the references to colour in this figure legend, the reader is referred to the web version of this article.)

(Z) directions. It is observed that the RLV remains within this mating zone for only 14 s. A docking maneuver could be attempted during this period. Since attempting a re-capture requires the ACCD to be partially winched back or redeployed to the required rope length, this 14 s window may be insufficient for a second attempt. Furthermore, previous studies [20,24] suggest that the ACCD typically requires around 15 s to execute a 15 m maneuver (in YZ plane), further reinforcing the conclusion that the available time may be too short for a second attempt.

Fig. 11 shows the profiles of the angle of attack and bank angle, along with their rates of change, which served as control inputs in the optimisation process. It can be observed that the control rates remain well within the imposed limits of $\pm 5°/\mathrm{s}$, and no significant sharp maneuvers are performed. This indicates that aggressive control inputs were not necessary, likely because the solution is already near the best achievable performance given the aerodynamic limitations.

This is further verified by examining the Hamiltonian and its partial derivatives with respect to the control rates. The Hamiltonian is a fundamental concept in optimal control theory, combining the system dynamics and running cost to evaluate necessary conditions for optimality [36]. It is defined as:

$$\mathcal{H}(x,u,\Lambda,t) = L(x,u,t) + \Lambda^T f(x,u,t) \tag{18}$$

where L is the running cost, f is the system dynamics, and Λ is the costate (adjoint) vector. According to Pontryagin's Minimum Principle, an optimal solution must minimize the Hamiltonian at each time with respect to the admissible control set, while satisfying all bounds, path constraints, and system dynamics. Since the control inputs ($\dot{\alpha}$ and $\dot{\sigma}$) affect only their corresponding integrator states (Eq. (9)), and the control

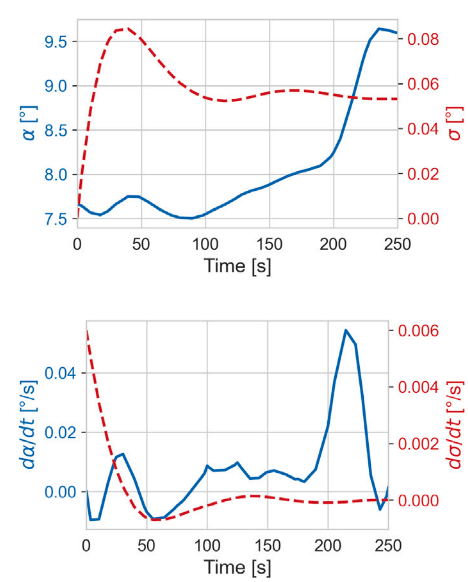

Fig. 11. Angle of attack and bank angle (top) with corresponding control rates (bottom) for RLV rendezvous in TA Case 1.

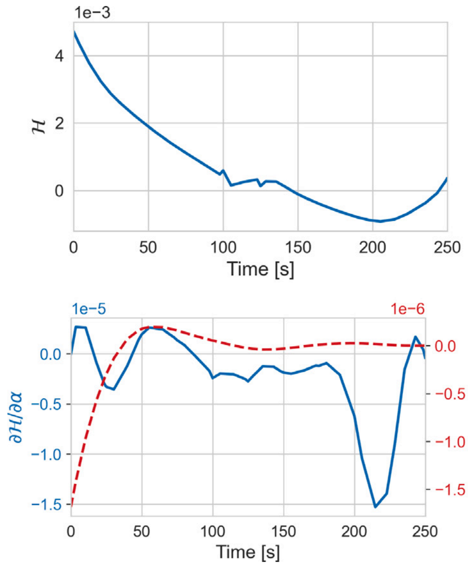

Fig. 12. Hamiltonian (top) and its partial derivatives with respect to control rates (bottom) for RLV rendezvous in TA Case 1.

cost is quadratic (Eq. (16)), the partial derivatives of the Hamiltonian simplify to:

$$\frac{\partial \mathcal{H}}{\partial \dot{\alpha}} = \Lambda_{\dot{\alpha}} + 2w_1\dot{\alpha} = 0 \tag{19}$$

$$\frac{\partial \mathcal{H}}{\partial \dot{\sigma}} = \Lambda_{\dot{\sigma}} + 2w_2\dot{\sigma} = 0 \tag{20}$$

This provides a means of verifying the optimality of the solution. As shown in Fig. 12, the Hamiltonian evolves smoothly over time. Although it is not constant — since the TA trajectory evolves over time and the final time is fixed — it varies in accordance with the TA trajectory through the cost function component J_1 given in Eq. (13). Additionally, the partial derivatives of the Hamiltonian with respect to the control rates remain close to zero (on the order of 10^{-5}), indicating that the necessary conditions for optimality are satisfied and the solution is near-optimal.

Although TA Case 1 was found to be suitable for only a single rendezvous attempt, this is not necessarily a negative outcome. High-precision guidance, navigation, and control (GNC) operations that rely on single-attempt execution have become increasingly common in modern spaceflight. For example, SpaceX's Falcon 9 boosters routinely perform autonomous, single-shot landings on both land-based pads and drone ships. More recently, SpaceX has introduced the "Mechazilla" launch tower system for its Starship program, which catches the returning booster with mechanical arms — again depending on highly accurate, one-attempt trajectories and timing. These examples highlight the feasibility and growing reliability of single-attempt precision maneuvers in real-world missions. Nonetheless, such a restriction does not apply to lifting-vehicle-based architecture, which can provide additional flexibility compared to vertical landing methods. In the context of 'In-Air Capturing', the option of a second attempt could be especially valuable. This highlights the importance of further developing RLV concepts that can provide additional lift and maneuvering margin to increase the opportunity for multiple capture attempts.

Case 2

Fig. 13 shows the rendezvous trajectory of the RLV with TA Case 2. Compared to Case 1, the altitude–velocity profile shows a greater overlap between the RLV and TA trajectories, owing to the closer aerodynamic performance between the two vehicles. As a result, TA Case 2 enables an extended formation flight phase — lasting up to 100 s — as indicated by the green-shaded region. This improvement is evident from the relative position and velocity of the RLV with respect to the TA.

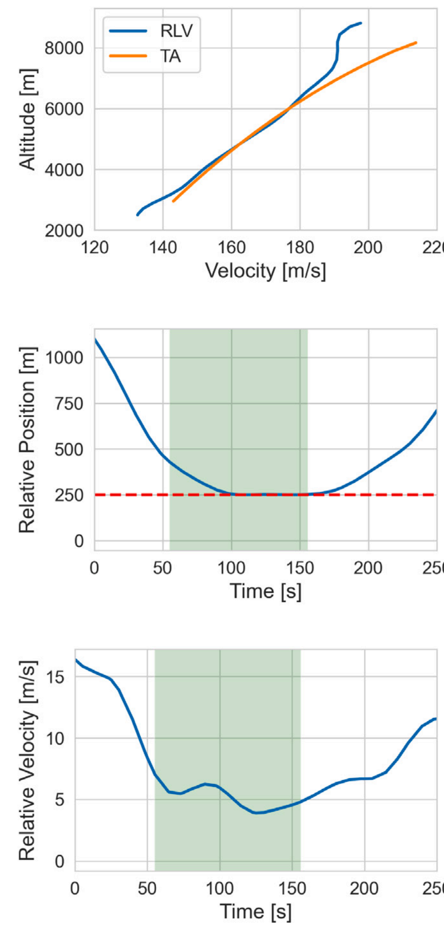

Fig. 13. Rendezvous trajectory simulation of the RLV with TA Case 2.

However, as shown in Fig. 14, the RLV remains within the mating zone for only 21 s, which does not represent a significant improvement over TA Case 1. Nonetheless, a margin exceeding 15 s could potentially allow for a second capture attempt toward the end of the formation flight — provided that no major uncertainties or anomalies occur.

As with TA Case 1, Fig. 15 also shows that the control rates remain well within the imposed ±5°/s limits, with no sharp or abrupt maneuvers observed. In conclusion, minimal control effort was sufficient to achieve the desired trajectory within aerodynamic constraints. Lastly, Fig. 16 confirms that the solution is near-optimal, as the partial derivatives of Hamiltonian with respect to the control rates remain close to zero throughout the trajectory.

Case 3

TA Case 3, having aerodynamic characteristics very similar to the RLV between angles of attack of 6° and 8°, is expected to yield the most favourable results. Fig. 17 shows a substantial overlap in the altitude–velocity profile between the two vehicles. Additionally, a formation flight duration of approximately 190 s can be observed from the relative position and velocity data. The RLV is able to closely match the TA's velocity, allowing it to maintain formation for an extended period.

However, the duration of formation flight is primarily limited by the lower aerodynamic performance of TA Case 3, which results in a steep descent along a flight path angle of approximately −8.5°. Consequently, the vehicles lose altitude rapidly, and the available time between the defined altitude corridor of 8000 m to 3000 m is significantly reduced.

Fig. 18 shows a smooth and controlled approach of the RLV into the mating zone, where it remains for nearly the entire duration of the

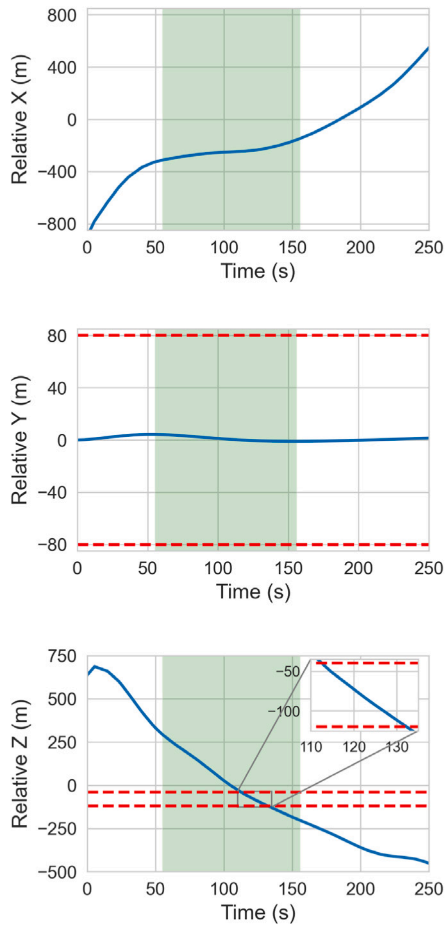

Fig. 14. Position of RLV relative to TA Case 2 with mating zone (red-dash). (For interpretation of the references to colour in this figure legend, the reader is referred to the web version of this article.)

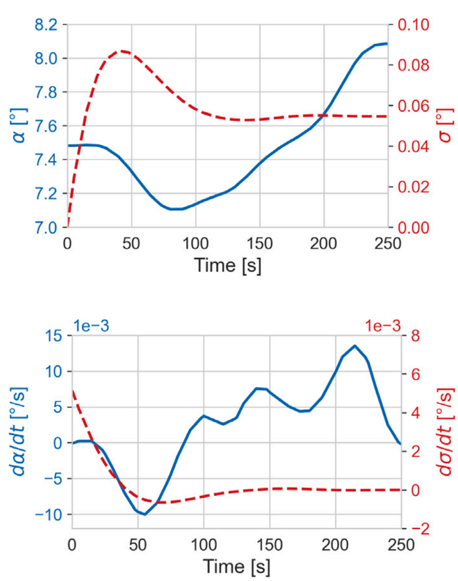

Fig. 15. Angle of attack and bank angle (top) with corresponding control rates (bottom) for RLV rendezvous in TA Case 2.

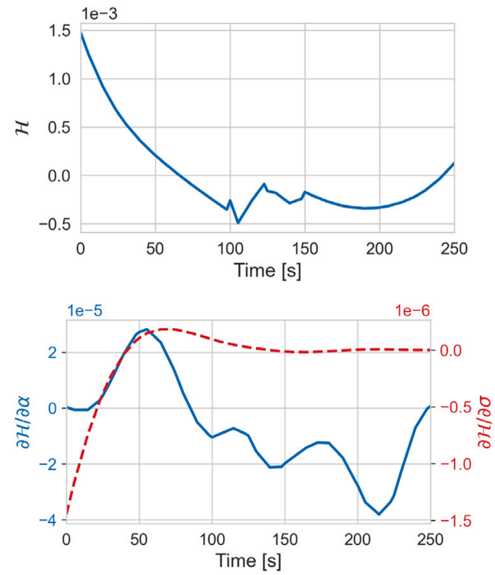

Fig. 16. Hamiltonian (top) and its partial derivatives with respect to control rates (bottom) for RLV rendezvous in TA Case 2.

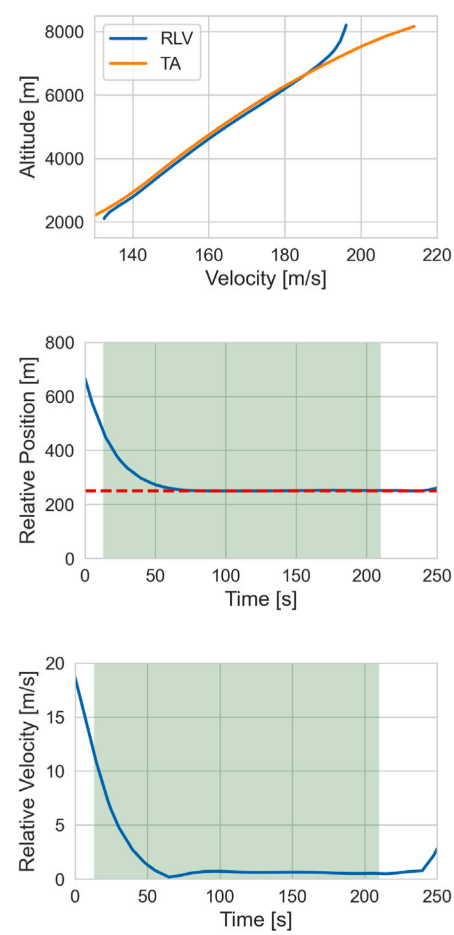

Fig. 17. Rendezvous trajectory simulation of the RLV with TA Case 3.

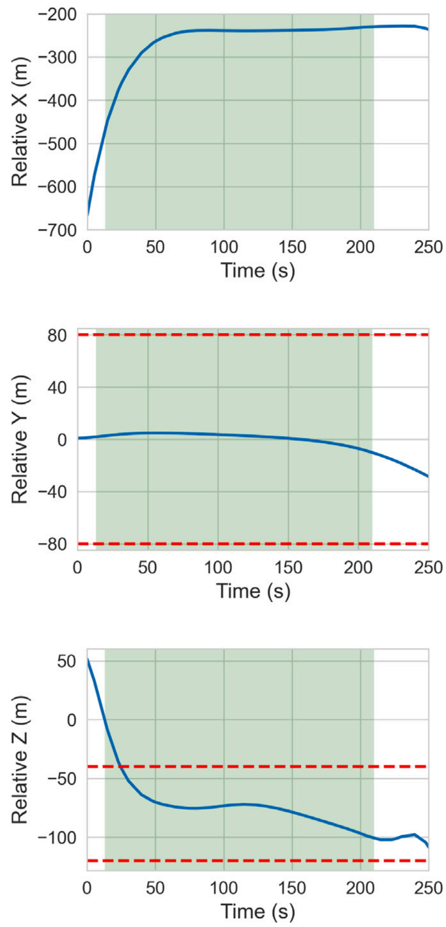

Fig. 18. Position of RLV relative to TA Case 3 with mating zone (red-dash). (For interpretation of the references to colour in this figure legend, the reader is referred to the web version of this article.)

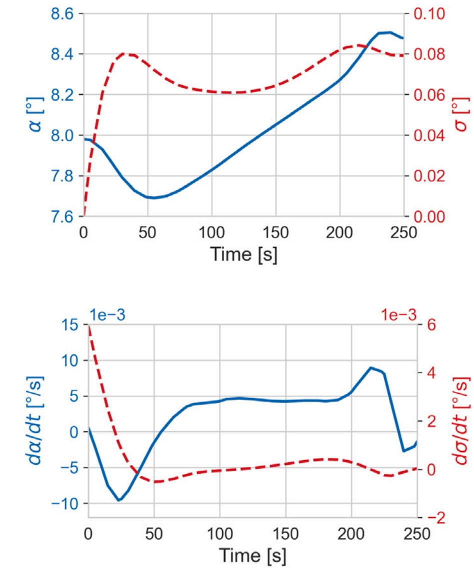

Fig. 19. Angle of attack and bank angle (top) with corresponding control rates (bottom) for RLV rendezvous in TA Case 3.

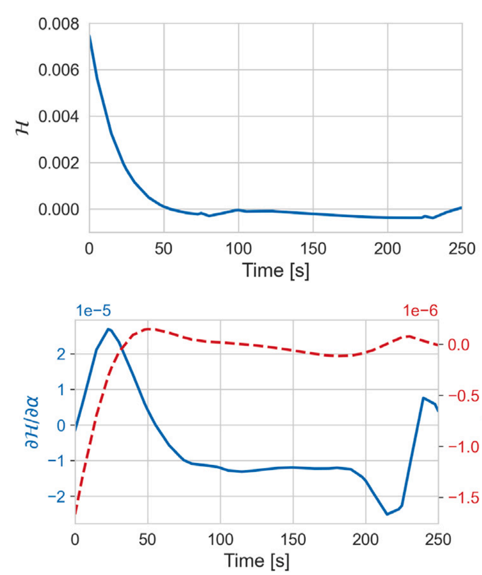

Fig. 20. Hamiltonian (top) and its partial derivatives with respect to control rates (bottom) for RLV rendezvous in TA Case 3.

formation flight. With a prolonged 150 s window inside the mating zone — and a steady relative position maintained at approximately 250 m, as shown in Fig. 17 — multiple docking attempts (two or more) become feasible. While achieving the aerodynamic performance of TA Case 3 with a conventional commercial aircraft may be unrealistic, the case serves to validate the underlying principle of 'In-Air Capturing': the closer the aerodynamic match between the two vehicles, the longer the available window for executing the capture maneuver.

Similar to the other two scenarios, no significant control effort was required for the rendezvous maneuver as it can be seen in Fig. 19. Lastly, the evolution of the Hamiltonian and its partial derivatives with respect to the control rates, shown in Fig. 20, further indicate that the solution is near-optimal.

4. Closed-loop simulations

The optimized RLV trajectory in the previous section serves as guidance throughout the rendezvous (formation flight and capture) of the RLV. However, the trajectory is optimized without accounting for uncertainties or external disturbances present in real-world dynamics. Therefore, closed-loop simulations are essential to assess its trackability and robustness under realistic operating conditions. In the present study, only the RLV trajectory corresponding to TA Case 2 is analysed, as it represents a more realistic scenario. It enables the investigation of both single- and multi-attempt recovery strategies without relying on the overly optimistic aerodynamic performance assumptions required in TA Case 3.

Since both vehicles are in a gliding descent during the rendezvous, the flight conditions evolve continuously. Additionally, external disturbances such as wind and aircraft wake can significantly influence the RLV's trajectory. Therefore, a reliable and adaptive control strategy is required to ensure accurate tracking of the guidance trajectory. Section 4.1 presents the overall closed-loop system architecture. To evaluate controller performance, open-loop and closed-loop simulations are compared in the presence of disturbances and modelling uncertainties in Section 4.2. Lastly, a Monte Carlo analysis is conducted to establish feasibility boundaries and re-planning criteria for the proposed guidance and control scheme in Section 4.3.

4.1. System architecture

Fig. 21 shows an outlook of the system architecture that is used in the current study. The system can be divided into three main components: the optimized RLV trajectory serving as guidance, the RLV plant

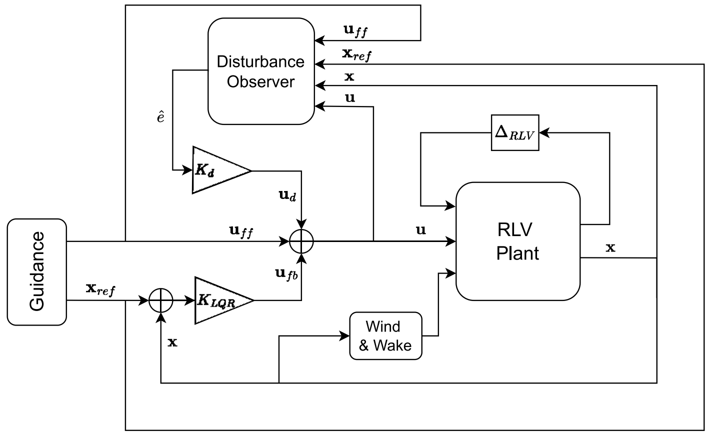

Fig. 21. Closed-loop system architecture for the RLV.

model incorporating disturbances and uncertainties, and a controller for tracking and disturbance rejection.

The RLV dynamics are modelled using the same point-mass equations of motion presented in Section 3.1. Additional atmospheric and environmental perturbations — namely wind, wake, and atmospheric density variations — as well as system uncertainties such as deviations in aerodynamic coefficients, are incorporated to reflect more realistic operating conditions. Wind is a major source of uncertainty for unpowered vehicles during precision maneuvers like 'In-Air Capturing'. To represent realistic conditions, this study employs the empirical HWM07 model via a MATLAB–Simulink package, which provides altitude-dependent wind profiles from decades of atmospheric data with good accuracy and computational efficiency [37].

As discussed in Section 2.2, the wake influences the RLV during its approach to the mating zone. From previous work [19], a disturbance database was generated at a single flight point (6000 m altitude, 142.39 m/s) for angles of attack between 0° and 10°. The model provides air-relative velocity changes and turbulent kinetic energy through position-based look-up tables, with superimposed time-dependent fluctuations to represent turbulence. Since wake data at multiple flight conditions are unavailable, the effect is assumed constant along the trajectory. In reality, the intensity and structure of the wake would vary with factors such as air density, altitude, and flight speed. A detailed overview of the wind and wake modelling is given in [23].

Lastly, uncertainty in atmospheric density is modelled using a normal distribution with a 3σ variation of 15%, while a 10% 3σ distribution is applied to the lift and drag coefficients.

The control input, as it can be observed from Fig. 21 has three main components:

- *Feed-forward control*: The nominal guidance trajectory for RLV is optimized to maximise time in the mating zone, incorporating key maneuvers critical to mission success. The corresponding control inputs (given by Eq. (9)) are applied as feed-forward control component ($\mathbf{u}_{\mathbf{ff}}$), preserving the trajectory shape and eliminating steady-state errors under ideal conditions.
- *Feed-back control*: A gain-scheduled Linear Quadratic Regulator (LQR) is employed to compensate for deviations from the nominal trajectory. This feedback control ($\mathbf{u}_{\mathbf{fb}}$) addresses tracking errors that may arise due to off-nominal initial conditions and external factors. Since mechanical energy plays a critical role in the behaviour of an unpowered RLV with limited aerodynamic control authority, gain scheduling is performed as a function of the system's total mechanical energy per unit mass.
  The nonlinear system is linearised at each operating point using the small-perturbation finite-difference method [38]. The operating points used for gain scheduling are described in [23]. At each operating point, the LQR gain matrix $\mathbf{K}_{LQR,i}$ is computed by solving the continuous-time Algebraic Riccati Equation [39]. The objective is to minimize the following cost function:

$$J = \int_0^\infty \left(\tilde{\mathbf{x}}^\top \mathbf{Q}\tilde{\mathbf{x}} + \tilde{\mathbf{u}}^\top \mathbf{R}\tilde{\mathbf{u}}\right) dt \tag{21}$$

where $\tilde{\mathbf{x}}$ is the deviation from the reference state, $\tilde{\mathbf{u}}$ is the deviation from the reference control, $\mathbf{Q} \geq 0$ is the state weighting matrix, and $\mathbf{R} > 0$ is the control weighting matrix given by:

$$\mathbf{R} = \text{diag}(2 \times 10^5,\ 2 \times 10^5) \tag{22}$$

$$\mathbf{Q} = \text{diag}(1.5 \times 10^{-5},\ 0.1,\ 0.075,\ 0.05,\ 10^4,\ 10^4,\ 10^6,\ 5000) \tag{23}$$

The optimal feedback gain $\mathbf{K}_i$ is obtained by first solving the Algebraic Riccati Equation:

$$\mathbf{A}_i^\top \mathbf{P}_i + \mathbf{P}_i \mathbf{A}_i - \mathbf{P}_i \mathbf{B}_i \mathbf{R}^{-1} \mathbf{B}_i^\top \mathbf{P}_i + \mathbf{Q} = 0 \tag{24}$$

where $\mathbf{P}_i$ is the unique positive semi-definite solution. The corresponding LQR gain is then given by:

$$\mathbf{K}_{LQR,i} = \mathbf{R}^{-1}\mathbf{B}_i^\top \mathbf{P}_i \tag{25}$$

This procedure is repeated for all $i = 1, \ldots, N$, resulting in a library of gain matrices for distinct operating points along the trajectory. These are used in the gain-scheduled controller based on the current energy state of RLV. It is assumed that the full state vector is measurable and available for feedback. Hence, the expression of the feedback control becomes:

$$\mathbf{u}_{\mathbf{fb}}(t) = -\mathbf{K}_{LQR,i}(E(t))\left(\mathbf{x}(t) - \mathbf{x}_{ref}(t)\right) \tag{26}$$

The controller takes as input the current state $\mathbf{x}(t)$ (Eq. (10)), which includes the effects of external disturbances and uncertainties, and compares it with the state from the optimized guidance trajectory $\mathbf{x}_{ref}(t)$ for Case 2, which represents the nominal state at a given time point. The controller output $\mathbf{u}_{\mathbf{fb}}$ consists of the resulting rates (shown in Eq. (9)), which compensate for trajectory tracking errors.
- *Disturbance rejection*: Prior work has shown that wind and wake cause significant disturbances in the RLV trajectory, leading to missed arrivals at the mating zone [23]. These deviations cannot be sufficiently compensated for by a nominal LQR alone due to model mismatch and the absence of disturbance estimation. To address this limitation, a Kalman filter-based residual-feedback scheme is used for disturbance rejection.
  To achieve this, at each time step k, the state and control deviations from the reference trajectory are first computed as follows:

$$\mathbf{x}_{\text{dev},k} = \hat{\mathbf{x}}_k - \mathbf{x}_{\text{ref},k} \tag{27}$$

$$\mathbf{u}_{\text{dev},k} = \mathbf{u}_k - \mathbf{u}_{\text{ff},k} \tag{28}$$

where $\hat{\mathbf{x}}_k$ is the current estimate of the state. For the initial time step ($k = 0$), the estimated state is assumed to be equal to the measured states of the non-linear plant $\mathbf{x}_k$. $\mathbf{x}_{\mathrm{ref},k}$ and $\mathbf{u}_{\mathrm{ff},k}$ represents the reference state and feed forward control input from the optimized guidance trajectory at time step k. $\mathbf{u}_k$ represents the total control input. Hence, these four elements serve as an input to the disturbance rejection block as shown in Fig. 21.

Based on the energy of the system at the current time step, the predicted next state estimate (before measurement update) is obtained from the discrete-time linearised model given by:

$$\hat{\mathbf{x}}_{k+1|k} = \mathbf{A_d}\,\mathbf{x}_{\mathrm{dev},k} + \mathbf{B_d}\,\mathbf{u}_{\mathrm{dev},k} + \mathbf{x}_{\mathrm{ref},k} \tag{29}$$

In parallel, the true nonlinear dynamics of the plant are propagated using the control input $\mathbf{u}_k$ through a fourth-order Runge–Kutta (RK4) integration and the resulting state $\mathbf{x}_{k+1}$ is used in the calculation of the residual. The residual, representing the mismatch between the propagated true state and its predicted estimate, is then computed as

$$\hat{e}_k = \mathbf{x}_{4:6,\,k+1} - \hat{\mathbf{x}}_{4:6,\,k+1}. \tag{30}$$

In this implementation, the residual is formed from the fourth to sixth components of the state vector, which correspond to the measured velocity (v), flight-path angle (γ), and azimuth (ψ). These states are selected because they are expected to be the most sensitive to wind and wake effects. The resulting residual acts as a proxy for external disturbances, capturing the combined effects of wind, wake, and other modelling uncertainties [40], and serves as an output to the disturbance observer block.

Inside the disturbance observer, the residual is also used for typical Kalman state propagation and update process to obtain the next state estimate (equations available in [41]). The initial error covariance **CovP**, process noise covariance **CovQ**, and measurement noise covariance **CovR** matrices are defined as:

$$\mathbf{CovP} = \mathrm{diag}\left(10^3,\ 0.1,\ 0.1,\ 10,\ 0.1,\ 0.1,\ 0.1,\ 0.1\right)$$

$$\mathbf{CovQ} = \mathrm{diag}\left(10^{-5},\ 10^{-5},\ 10^{-5},\ 10^{-6},\ 10^{-6},\ 10^{-6},\ 10^{-5},\ 10^{-5}\right)$$

$$\mathbf{CovR} = \mathrm{diag}\left(0.1^2,\ 0.001^2,\ 0.001^2\right)$$

An energy-scheduled gain ($\boldsymbol{K_d}$) is applied to the residual ($\hat{e}$) output and fed back to the system as the control component $\mathbf{u_d}$.

$$\boldsymbol{u_d} = \boldsymbol{K_d}.\hat{e} = \boldsymbol{K_d}.(\mathbf{x} - \hat{\mathbf{x}}) \tag{31}$$

Here, the energy-scheduled gain $\boldsymbol{K_d}$ is obtained from a linear quadratic regulator (LQR) design, where the weighting matrices are defined as

$$\mathbf{Q_w} = \mathrm{diag}(0,\ 0,\ 0,\ 0.0001,\ 0.1,\ 0.01,\ 0.001,\ 0.001)$$

and

$$\mathbf{R_w} = \mathrm{diag}\left(2\times 10^6,\ 2\times 10^6\right),$$

The structure is similar to a Luenberger observer [42] but incorporates a Kalman filter to separate high-frequency content (e.g., measurement noise and uncertainty in air density and aerodynamic coefficients) from lower-frequency wind and wake effects. This provides disturbance rejection that a nominal LQR cannot achieve.

4.2. Closed loop performance

This section assesses the performance of the closed-loop system in the presence of external disturbances (wake and wind) as well as the modelling uncertainties (atmospheric density and aerodynamic coefficients). Closed-loop LQR with disturbance rejection (CL w DR) is compared against a nominal LQR without disturbance rejection (CL w/o DR) and an open-loop, feed-forward only configuration (OL).

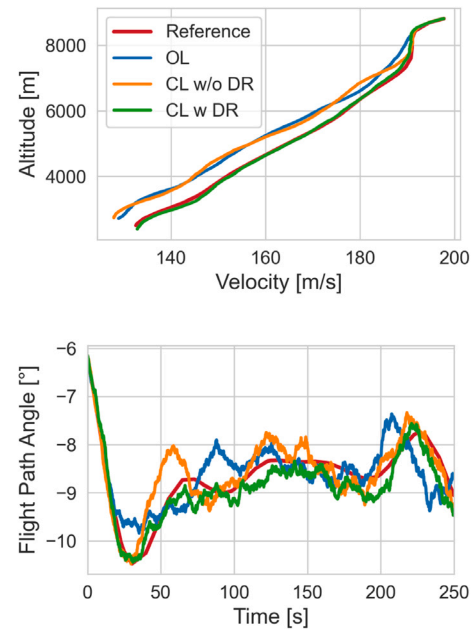

Fig. 22. RLV rendezvous in TA Case 2-closed-loop performance with and without disturbance rejection compared to open-loop.

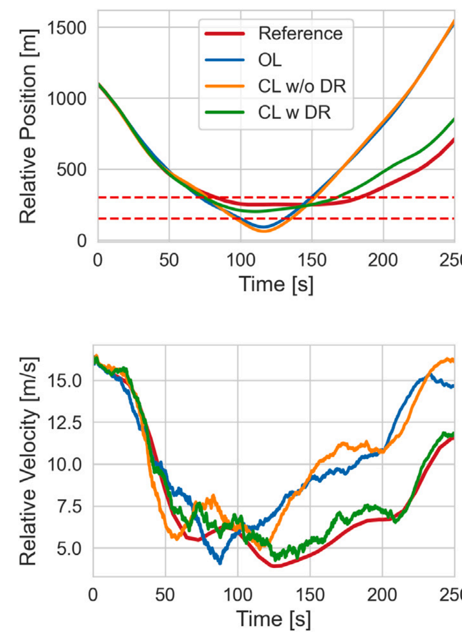

Fig. 23. RLV state relative to TA Case 2-closed-loop performance with and without disturbance rejection compared to open-loop.

Figs. 22 and 23 show the RLV state for all the three configurations along with the original reference designed for TA Case 2.

From Fig. 22, it can be observed that the open-loop and the closed-loop without disturbance rejection cannot maintain the reference altitude and velocity, while the inclusion of disturbance rejection provides satisfactory tracking performance. Examining the flight path angle evolution over time shows that the selected closed-loop with disturbance rejection achieves the closest tracking while avoiding amplification of low-frequency, uncertainty-driven disturbances. Next, from Fig. 23, the RLV's relative position with respect to the TA remains within the mating zone (dashed red bounds) only when disturbance rejection is included; the open-loop and nominal LQR cases cannot hold their position

Table 4
3σ dispersions in initial states for Monte Carlo analysis.

State	Dispersion
Distance North [m]	±150
Distance East [m]	±150
Distance Down [m]	±150
Speed [m/s]	±20
Azimuth angle [°]	±1
Flight-path angle [°]	±1
Angle of attack [°]	±2
Bank angle [°]	±2

Table 5
Uncertainties for Monte Carlo analysis.

Uncertainty	Dispersion
Mass [kg]	±7000
Atmospheric density [%]	±15
Drag coefficient [%]	±10
Lift coefficient [%]	±10
Wind	HWM07
Other disturbances	Aircraft Wake

within the bounds. The selected controller also maintains the relative velocity close to the reference, whereas the other configurations show substantial deviations over time.

Hence, the inclusion of disturbance rejection with LQR provides the required performance to reach the mating zone, making capture feasible. This architecture will serve as the baseline for the Monte Carlo analysis in the coming subsection.

4.3. Monte Carlo campaign

A Monte Carlo analysis is essential to understand the feasibility boundaries and re-planning criteria for the proposed guidance trajectory and control scheme. By evaluating performance under realistic variations in initial conditions and environmental disturbances, the study provides a statistical assessment of robustness outside the nominal scenario. Table 4 presents the range of initial state dispersions used in the study, defined as the 3σ bounds of a normal distribution. The position errors are introduced in the NED (North-East-Down) coordinate frame for easier interpretation and clearer physical understanding of the deviations from the nominal initial state used in the reference trajectory. Furthermore, the external disturbances and model uncertainties mentioned previously are also included and summarized in Table 5. A trajectory is considered feasible if it arrives within the bounds of the mating zone. It is assumed that the tether length can vary between 150 m and 300 m using a winch mechanism, and any trajectory that reaches this relative position with a relative velocity less than 10 m/s behind the aircraft is considered feasible for capture.

Fig. 24 shows the Monte Carlo distribution of 1000 closed-loop successful trajectories in comparison to the nominal reference trajectory. While the guidance and control system enabled many successful outcomes, the overall closed loop success rate was only 30.75% (in a sample of 3252 cases), with the initial error bounds defined in Table 4. Further investigation is required to identify the feasible conditions that yield a consistently high success rate.

Fig. 25 shows the Monte Carlo distribution of successful cases plotted against initial altitude and initial velocity. The colour of each scatter point represents the time spent in the mating zone. Trajectories that spend 15 s or more in the mating zone are assumed to allow for multiple capture attempts by the capturing device, while shorter durations correspond to only a single attempt. From the figure, it can be observed that most successful trajectories that allow for multiple capture attempts tend to have higher velocities compared to single attempt cases. This is consistent with residual wind and wake effects that could bias the

Table 6
Dispersion distribution by radius for 1000 successful cases.

Radius [m]	0–50	50–100	100–150	> 150
Single attempt	304	277	58	2
Multiple attempts	179	158	21	1
Total	483	435	79	3

trajectory and reduce attainable velocity. Additionally, there appears to be a trade-off between altitude and velocity deviations — positive deviations in altitude require lower initial velocities, while negative deviations require higher velocities. This aligns with expectations, as the unpowered RLV must possess an appropriate amount of energy to successfully follow the guidance trajectory. If the total energy is either too high or too low, the guidance becomes infeasible. An additional finding is that successful cases occurred only when mass uncertainty remained within ±3000 kg; beyond this range, the resulting lift-to-weight mismatch — whether too low or too high — prevented tracking of the reference trajectory and made capture infeasible.

Fig. 26 shows the Monte Carlo dispersion over the radius of error sphere, plotted against the specific energy (energy per unit mass). The error sphere represents the magnitude of the initial position error in 3D space, combining deviations in the north, east, and down directions. It is given by:

$$r_{error} = \sqrt{\Delta x_{north}^2 + \Delta y_{east}^2 + \Delta z_{down}^2}$$

where r_{error} gives the scalar distance from the nominal initial position. The scattered points in Fig. 26 represent successful closed-loop trajectories, colour-coded based on the time spent in the mating zone. The figure shows that successful trajectories with initial errors tend to cluster near the nominal point, both in terms of energy and positional accuracy. This indicates that maintaining initial conditions within a bounded region around the nominal state in both energy and spatial error could improve the chances of successful capture. Table 6 further quantifies the relationship between the time spent in the mating zone and the magnitude of the initial spatial error at the start of the maneuver.

Based on Fig. 26 and Table 6, feasibility can be significantly improved by constraining the initial error sphere radius to within 100 m and the error in specific energy to within ±1% of the nominal value. Further, the mass uncertainty is limited to within ±3000 kg When the MC simulations were repeated under these constraints, the closed-loop success rate increased to 91.4%. This result provides a basis for defining a trajectory replanning criterion — if the initial spatial and energy errors exceed the specified bounds, a new guidance trajectory must be computed to ensure successful rendezvous. Alternatively, improved results can be achieved by making greater efforts to align the aerodynamic behaviour of the TA with that of the RLV (or vice versa), as demonstrated in Case 3.

5. Conclusion

This study develops a guidance and control framework for the rendezvous trajectory of a reusable launch vehicle (RLV) intended to be captured mid-air by a towing aircraft within the 'In-Air Capturing' concept. During this process, the RLV must execute a precise rendezvous maneuver and maintain stable formation within a designated, wake-free mating zone behind the aircraft, where a tethered capturing device is deployed in advance and awaits connection. The conditions required for successful capture — namely maintaining safe separation from the towing aircraft, remaining within the operational range of the capturing device, and minimising relative velocity during final approach — were formally defined as formation flight criteria. These requirements were then incorporated into the formulation of an optimal control problem, which was solved using a general-purpose pseudospectral method. This

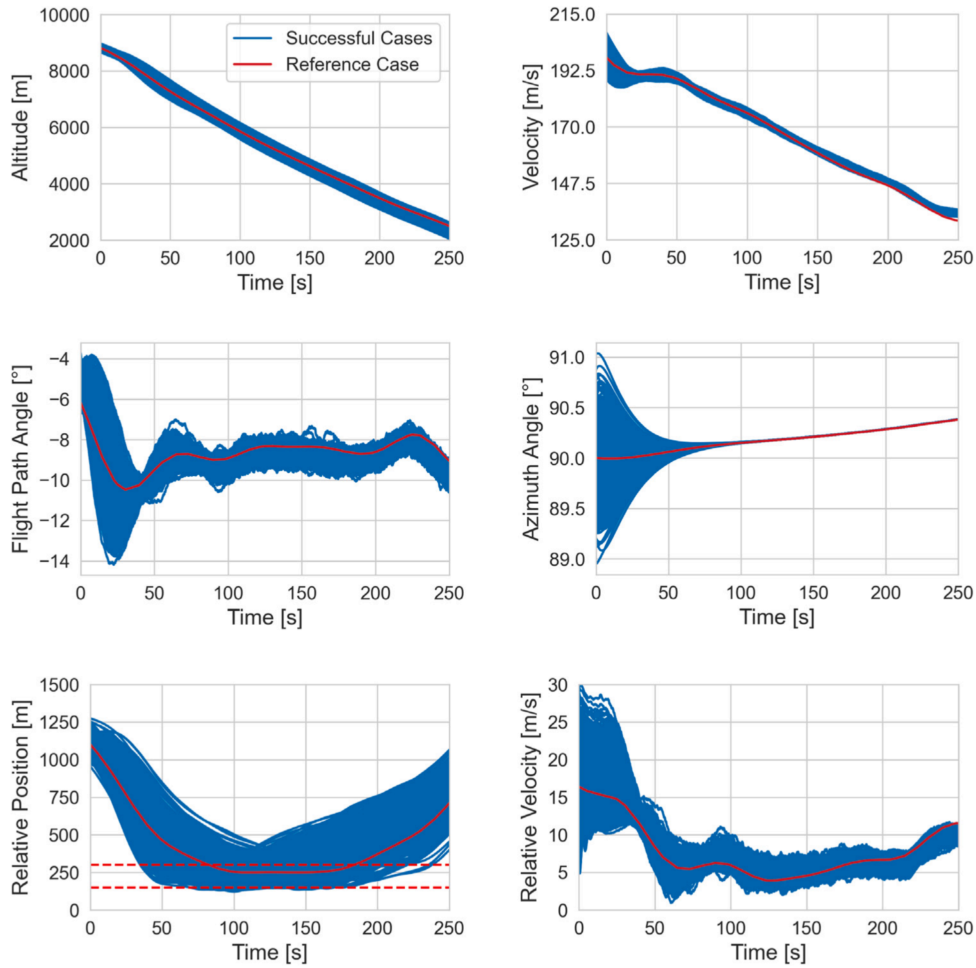

Fig. 24. Trajectory simulations of the RLV — Monte Carlo Distribution.

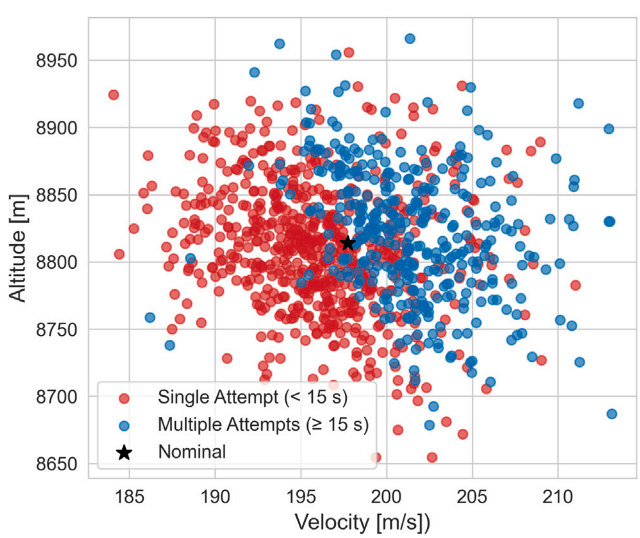

Fig. 25. Monte Carlo Distribution: Effect of initial velocity and altitude on mating time.

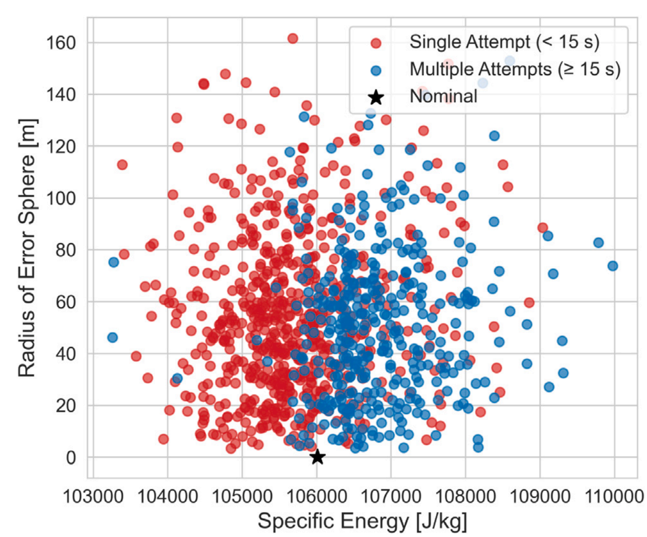

Fig. 26. Monte Carlo Distribution: Effect of position error and energy on mating time.

approach provides fast and reliable solutions, making it particularly well suited for trajectory optimisation in guidance applications.

The optimized trajectories were subsequently employed as references in a closed-loop guidance and control system. A gain-scheduled Linear Quadratic Regulator (LQR) was designed to provide stability and accurate trajectory tracking across varying flight conditions. In addition, a disturbance-rejection mechanism was incorporated to mitigate the adverse effects of wind, and aircraft wake. Closed-loop performance was evaluated through simulations, and robustness was further assessed using Monte Carlo analysis. The results show that while successful capture may be achieved within a single attempt, the framework supports multiple attempts within the mating zone, thereby increasing operational reliability. Moreover, by introducing a final re-planning criterion based on the vehicle's energy and position error radius, the probability of successful capture was improved to 91.4%. Overall, the developed guidance–control framework, together with the accompanying feasibility analysis, represents a step toward establishing 'In-Air Capturing' as a practical recovery approach for future reusable launch systems.

Future work will focus on the design and implementation of the guidance, navigation, and control (GNC) system for the autonomous capturing device, with particular emphasis on establishing robust communication and coordination with the RLV to ensure reliable final docking. Before moving to flight trials, the feasibility of the capture maneuver will be re-assessed through full scale simulations, allowing system requirements to be refined and robustness to be verified under a wide range of operating conditions and disturbances. A subsequent milestone will be the in-flight sub-scale demonstration of the complete capture process, in which an autonomous capturing device — towed by a towing aircraft demonstrator during descent — connects with a descending RLV demonstrator. This demonstration could be pursued as a follow-up to the H2020 project FALCon, which previously investigated the 'In-Air Capturing' concept through lab-scale UAV (below 100 kgs) flights. Achieving such a demonstration will represent a decisive step in validating the practical feasibility of 'In-Air Capturing' under realistic conditions.

CRediT authorship contribution statement

Sunayna Singh: Writing – review & editing, Writing – original draft, Visualization, Validation, Software, Methodology, Investigation, Formal analysis. **Marco Sagliano:** Supervision.

Declaration of competing interest

The authors declare that they have no known competing financial interests or personal relationships that could have appeared to influence the work reported in this paper.

References

[1] Verfahren zum Bergen einer Stufe eines mehrstufigen Raumtransportsystems, 2003, DE 101 47 144 C1.

[2] M. Sippel, S. Singh, S. Stappert, RLV-return mode "In-Air-Capturing" and definition of its development roadmap, in: 9th European Conference on Aeronautics and Space Sciences, EUCASS, 2022.

[3] I. Dietlein, L. Bussler, S. Stappert, J. Wilken, M. Sippel, et al., Overview of system study on recovery methods for reusable first stages of future European launchers, CEAS Space J. 17 (71) (2024) 71–88, http://dx.doi.org/10.1007/s12567-024-00557-9.

[4] O. Godet, J. Mansouri, J. Breteau, A.P. de Mirand, E. Louaas, Launch vehicle system studies in the "future launchers preparatory programme": the reusability option for ariane evolutions, in: 8th European Conference for Aeronautics and Space Science, EUCASS, 2019, http://dx.doi.org/10.13009/EUCASS2019-971.

[5] I. Dietlein, L. Bussler, S. Stappert, J. Wilken, M. Sippel, Overview of system study on recovery methods for reusable first stages of future European launchers, CEAS Space J. (2024) 1–18.

[6] J. Wilken, M. Herberhold, M. Sippel, Options for future European reusable booster stages: evaluation and comparison of VTHL and VTVL costs, CEAS Space J. 17 (1) (2025) 177–198.

[7] G.J.D. Calabuig, A. Wilson, S. Bi, M. Vasile, M. Sippel, M. Tajmar, Environmental life cycle assessment of reusable launch vehicle fleets: Large climate impact driven by rocket exhaust emissions, Acta Astronaut. 221 (2024) 1–11, http://dx.doi.org/10.1016/j.actaastro.2024.05.009.

[8] M. Herberhold, J. Wilken, M. Sippel, Impact of engine cycles, propellants and recovery methods on the launch exhaust profile of reusable booster stages, in: 11th European Conference on Aeronautics and Space Sciences, EUCASS, 2025.

[9] A.S. Hameed, G. Bindu, Gain scheduled finite horizon LQR for approach and landing phase of a reusable launch vehicle, J. Inst. Eng. (India): Ser. C 103 (3) (2022) 381–388.

[10] Z. Wang, U. Montanaro, S. Fallah, A. Sorniotti, B. Lenzo, A gain scheduled robust linear quadratic regulator for vehicle direct yaw moment control, Mechatronics 51 (2018) 31–45.

[11] G. Dukeman, Profile-following entry guidance using linear quadratic regulator theory, in: AIAA Guidance, Navigation, and Control Conference and Exhibit, 2002, p. 4457.

[12] W. Zhou, S. Tan, H. Chen, A simple reentry trajectory generation and tracking scheme for common aero vehicle, in: AIAA Guidance, Navigation, and Control Conference, 2012, p. 4709.

[13] S. Singh, S. Stappert, S. Buckingham, S. Lopes, Y.C. Kucukosman, M. Simioana, P. Planquart, Dynamic modelling and control of an aerodynamically controlled capturing device for 'In-Air-Capturing' of a reusable launch vehicle, in: 11th International ESA Conference on Guidance, Navigation and Control Systems, 2021.

[14] S. Singh, S. Stappert, L. Bussler, M. Sippel, Y.C. Kucukosman, S. Buckingham, Full-scale simulation and analysis of formation flight during In-Air Capturing of a winged reusable launch vehicle, J. Space Saf. Eng. 9 (4) (2022) 541–552.

[15] S. Stappert, S. Singh, M. Sippel, Developing an innovative and high-performance method for recovering reusable launcher stages: The In-Air Capturing method, CEAS Space J. (2023) http://dx.doi.org/10.1007/s12567-023-00512-0.

[16] S. Singh, L. Bussler, K. Bergmann, M. Sippel, Mission design and sensitivity analysis for In-Air Capturing of a winged reusable launch vehicle, in: Proceedings of 74th International Astronautical Congress, 2019.

[17] M. Sippel, S. Stappert, L. Bussler, C. Messe, Powerful and flexible future launchers in 2- or 3-stage configuration, in: Proceedings of 70th International Astronautical Congress, 2019.

[18] G. Norris, M. Wagner, Airbus A340 and A330 (Jetliner History), Zenith Imprint, 2001.

[19] Y.C. Kucukosman, S. Lopes, S. Buckingham, P. Planquart, S. Singh, L. Bussler, S. Stappert, M. Sippel, Aerodynamic characterization of in-air capturing vehicles using CFD simulations, in: 9th European Conference on Aeronautics and Space Sciences, EUCASS, 2022.

[20] S. Singh, M. Mastrogiuseppe, Multibody modelling of tether and capture system for dynamic simulations of In-Air Capturing, Acta Astronaut. 218 (2024) 59–69, http://dx.doi.org/10.1016/j.actaastro.2024.02.008.

[21] L. Briek, ICARUS: In-Air Capturing Apparatus for Recovering Unpropelled Stages (Masters thesis), Delft University of Technology, 2024.

[22] B. Luyten, S. Singh, B. Zandbergen, Designing an electromechanical capture system for In-Air Capturing of winged RLVs, CEAS Space J. (2025) http://dx.doi.org/10.1007/s12567-025-00660-5.

[23] S. Singh, M. Sagliano, Gain-scheduled LQR for RLV during In-Air Capturing: trajectory tracking, recovery limits and replanning criteria, in: 11th European Conference on Aeronautics and Space Sciences, EUCASS, 2025.

[24] S. Singh, M. Simioana, S. Stappert, M. Sippel, S. Buckingham, S. Lopes, Y.C. Kucukosman, Control design and analysis of a capturing device performing In-Air Capturing of a reusable launch vehicle, in: 9th European Conference on Aeronautics and Space Sciences, EUCASS, 2022.

[25] S. Singh, B. Luyten, M. Sagliano, Relative navigation implementation for the In-Air Capturing of a winged reusable launch vehicle, in: 3rd International Conference on High-Speed Vehicle Science Technology, 2024.

[26] F. Fahroo, I.M. Ross, Advances in pseudospectral methods for optimal control, in: AIAA Guidance, Navigation and Control Conference and Exhibit, 2008, p. 7309.

[27] A.V. Rao, D.A. Benson, C. Darby, M.A. Patterson, C. Francolin, I. Sanders, G.T. Huntington, Algorithm 902: Gpops, a matlab software for solving multiple-phase optimal control problems using the gauss pseudospectral method, ACM Trans. Math. Softw. (TOMS) 37 (2) (2010) 1–39.

[28] M. Sagliano, Pseudospectral convex optimization for powered descent and landing, J. Guid. Control Dyn. 41 (2) (2018) 320–334.

[29] M. Sagliano, Development of a Novel Algorithm for High Performance Reentry Guidance (Ph.D. thesis), Universität Bremen, Bremen, Germany, 2016.

[30] L. Huneker, M. Sagliano, Y. Arslantas, Spartan: an improved global pseudospectral algorithm for high-fidelity entry-descent-landing guidance analysis, in: 30th ISTS, 2015.

[31] M.A. Patterson, A.V. Rao, GPOPS-II: A MATLAB software for solving multiple-phase optimal control problems using hp-adaptive Gaussian quadrature collocation methods and sparse nonlinear programming, ACM Trans. Math. Softw. (TOMS) 41 (1) (2014) 1–37.

[32] D. Garg, Advances in Global Pseudospectral Methods for Optimal Control (Ph.D. thesis), Massachusetts Institute of Technology, USA, 2011.

[33] N.X. Vinh, Optimal trajectories in atmospheric flight, in: Studies in Astronautics, vol. 2, Elsevier Scientific Publishing Company, 1981, p. 402.

[34] A.E. Bryson, Applied Optimal Control: Optimization, Estimation and Control, Routledge, 2018.

[35] E. Taheri, J.L. Junkins, Generic smoothing for optimal bang-off-bang spacecraft maneuvers, J. Guid. Control Dyn. 41 (11) (2018) 2470–2475.

[36] D.E. Kirk, Optimal Control Theory: An Introduction, Prentice Hall, Englewood Cliffs, NJ, 1970.

[37] D.P. Drob, J.T. Emmert, G. Crowley, J. Picone, G. Shepherd, W. Skinner, P. Hays, R.J. Niciejewski, M. Larsen, C.Y. She, et al., An empirical model of the Earth's horizontal wind fields: HWM07, J. Geophys. Res.: Space Phys. 113 (A12) (2008).

[38] H. Lee, Linearization of Nonlinear Control Systems, Springer, 2022.
[39] K. Ogata, Modern Control Engineering, Prentice Hall, 2009.
[40] S. Gillijns, B. De Moor, Unbiased minimum-variance input and state estimation for linear discrete-time systems, Automatica 43 (1) (2007) 111–116.
[41] R.E. Kalman, A new approach to linear filtering and prediction problems, J. Basic Eng. 82 (1) (1960) 35–45, http://dx.doi.org/10.1115/1.3662552.
[42] W. Xue, Z. Gao, On the augmentation of luenberger observer-based state feedback design for better robustness and disturbance rejection, in: 2015 American Control Conference, ACC, IEEE, 2015, pp. 3937–3943.